

Neutral B meson mixings and B meson decay constants with static heavy and domain-wall light quarks

Yasumichi Aoki,¹ Tomomi Ishikawa,² Taku Izubuchi,^{3,2} Christoph Lehner,³ and Amarjit Soni³

¹*Kobayashi-Maskawa Institute for the Origin of Particle and the Universe (KMI), Nagoya University, Nagoya 464-8602, Japan*

²*RIKEN BNL Research Center, Brookhaven National Laboratory, Upton, New York 11973, USA*

³*Physics Department, Brookhaven National Laboratory, Upton, New York 11973, USA*

(Dated: June 27, 2015)

Neutral B meson mixing matrix elements and B meson decay constants are calculated. Static approximation is used for b quark and domain-wall fermion formalism is employed for light quarks. The calculations are carried out on $2+1$ flavor dynamical ensembles generated by RBC/UKQCD Collaborations with lattice spacings 0.086 fm ($a^{-1} \sim 2.3$ GeV) and 0.11 fm (1.7 GeV), and a fixed physical spatial volume of about $(2.7 \text{ fm})^3$. In the static quark action, link-smearings are used to improve the signal-to-noise ratio. We employ two kinds of link-smearings, HYP1 and HYP2, and their results are combined in taking the continuum limit. For the matching between the lattice and the continuum theory, one-loop perturbative $O(a)$ improvements are made to reduce discretization errors. As the most important quantity of this work, we obtain SU(3) breaking ratio $\xi = 1.208(60)$, where the error includes statistical and systematic one. (Uncertainty from infinite b quark mass is not included.) We also find other neutral B meson mixing quantities $f_B \sqrt{\hat{B}_B} = 240(22)$ MeV, $f_{B_s} \sqrt{\hat{B}_{B_s}} = 290(22)$ MeV, $\hat{B}_B = 1.17(22)$, $\hat{B}_{B_s} = 1.22(13)$ and $B_{B_s}/B_B = 1.028(74)$, B meson decay constants $f_B = 219(17)$ MeV, $f_{B_s} = 264(19)$ MeV and $f_{B_s}/f_B = 1.193(41)$, in the static limit of b quark, which do not include infinite b quark mass uncertainty.

I. INTRODUCTION

Standard Model (SM) of elementary particles is consistent with all experimental data, so far. The SM, however, does not still satisfy us, because it cannot answer some of our basic questions, such as the reason why the gauge group, constituents of particles and number of generation in the model are chosen as they are, hierarchical unnaturalness in mass scales between three generation of fermions, and so on. While the existence of Higgs boson has been experimentally confirmed at Large Hadron Collider (LHC), expected new particles have not been discovered as yet. Thus bottom-up approaches toward physics beyond Standard Model (BSM) is becoming more and more important. In order to address BSM, precision tests for SM are highly meaningful. Combining theoretical predictions with the experimental results, it would be possible to obtain hints for the BSM. In such an attempt, the Cabibbo-Kobayashi-Maskawa (CKM) quark mixing matrix elements [1] play a crucial role to check the consistency of the SM.

In the SM, the transition of neutral B (B_s) meson to its anti-meson occurs via box diagrams involving exchange of two W -bosons and this amplitude would provide a clean determination for the matrix elements V_{td} and V_{ts} assuming V_{tb} is known. In the SM framework, dominant contribution to the mass difference of the neutral B meson mass eigenstates is related with the CKM matrix elements by

$$\Delta m_{B_q} = \frac{G_F^2 m_W^2}{16\pi^2 m_{B_q}} |V_{tq}^* V_{tb}|^2 S_0(x_t) \eta_B \hat{\mathcal{M}}_{B_q}, \quad (1)$$

where $q = \{d, s\}$. In Eq. (1), both the Inami-Lim function $S_0(x_t)$ ($x_t = m_t^2/m_W^2$) [2] and the QCD coefficient

η_B can be calculated perturbatively. $\hat{\mathcal{M}}_{B_q}$ is a renormalization group invariant (RGI) $\Delta B = 2$ four-fermion operator matrix element in an effective Hamiltonian of the box diagram at low-energy scale. The mixing matrix element $\hat{\mathcal{M}}_{B_q}$ is a highly nonperturbative quantity, thus currently the only possible method for a precise determination is via numerical lattice QCD simulations. By taking a ratio [3] of Eq. (1) between $q = d$ and s , we obtain

$$\left| \frac{V_{td}}{V_{ts}} \right| = \xi \sqrt{\frac{\Delta m_B}{\Delta m_{B_s}} \frac{m_{B_s}}{m_B}}, \quad (2)$$

where ξ is called SU(3) breaking ratio

$$\xi = \frac{m_B}{m_{B_s}} \sqrt{\frac{\mathcal{M}_{B_s}}{\mathcal{M}_B}}. \quad (3)$$

The ratio constrains the apex of the CKM unitary triangle and new quark-flavor-changing interactions from BSM would affect this quantity. In the ratio many uncertainties get canceled and precise determination of ξ would lead to a tight constraint on the CKM unitary triangle and hints for BSM physics as inconsistency of the unitary triangle in the SM.

Lattice QCD simulations including b quark are, however, quite challenging, because of the large scale difference between light quarks (u and d) and b quark. While fine lattice spacings are needed to correctly treat the b quark, the large volume is required to accommodate pion dynamics. Such a situation is difficult to achieve with the current computational ability. Heavy Quark Effective Theory (HQET) provides one realistic solution to this problem. In this formulation, the heavy (b) quark dynamics is integrated out and we may only treat the

dynamics associated with light quarks. The theory is described by systematic expansion of inverse of heavy quark mass m_Q . First attempt in this direction was carried out by Eichten and Hill [4, 5], in which they used static approximation (leading order of heavy quark mass expansion) and, for the static quark, they employed a standard static action. Soon after that attempt, however, it turned out that this approach leads to a poor signal-to-noise ratio (S/N) in correlation functions, because the static self-energy contains a notorious $1/a$ power divergence. (On the other hand, in Non-Relativistic QCD (NRQCD), another effective theory approach, the power divergence tends to be canceled [6].) This situation has been significantly improved since ALPHA Collaboration introduced link smearing technique in the static action, which partly cured the difficulty [7, 8].

In this paper, we calculate B meson decay constants and neutral B meson mixing matrix elements using the static approximation. The static approximation always has $O(\Lambda_{\text{QCD}}/m_b) \sim O(10\%)$ uncertainty, since physical b quark mass is not infinite. For SU(3) breaking ratios like ξ or the ratio of B meson decay constants, however, the uncertainty coming from the static approximation is down to around 2% level. This means the static limit could be especially good approximation compared with other lattice approaches that take into account b quark mass dependence for such ratios. To reduce the $O(\Lambda_{\text{QCD}}/m_b)$ uncertainty in the HQET approach, higher order operators in the $1/m_Q$ expansion need to be included. Taking into account these contributions requires nonperturbative matching with continuum using e.g. Schrödinger functional scheme with step scaling technique [10], which requires considerable effort. Instead, we stay in static limit assuming that the results can be valuable for interpolation to physical b quark mass combining with lighter quark mass simulations, for which high precision calculation is significantly important. (We discuss the meaning of calculations at the static limit in Sec. II.) This work is a first step toward the precise determination of B physics quantities in the static limit.

This paper is organized as follows. In Sec. II, we discuss the meaning of the calculations at the static limit as an anchor point in the study of heavy quark physics. In Sec. III, we summarize the physical observables both in QCD full theory and HQET side, which we address for the study of neutral B meson mixing phenomena. In Sec. IV, the definition of lattice actions and the gluon ensembles that we use in this study are explained. In Sec. V, we describe the matching procedure between QCD full theory and HQET in continuum, as well as between continuum and lattice in HQET. The HQET matching is carried out by one-loop perturbation including $O(a)$ lattice errors. In Sec. VI, details of the measurement, correlator fits and formula for constructing physical quantities are shown. In Sec. VII, chiral and continuum extrapolation formula (SU(2) χ PT) are summarized and we show the fit results. In Sec. VIII, we present the estimation of the systematic uncertainties and summarize

it in Tab. XII. Finally, we present final results, compare them with other works and discuss future direction of this project in Sec. IX.

II. STATIC LIMIT AS A STRONG ANCHOR POINT

We employ the static approximation as b quark treatment in this study. As discussed earlier, this approximation suffers from uncertainty of $O(10\%)$ for primary quantities or $O(2\%)$ for flavor SU(3) breaking ratios at the physical b quark mass, which is heavy but finite. The physical value of the approximation will eventually get lost as one aims higher and higher precision. The results at the static limit is, however, valuable as an anchor point when combined with simulations in lower quark mass region. In this section we clarify the meaning of our calculations at the static limit.

We consider a heavy quark expansion of some heavy-light quantity Φ_{hl} , which has a finite asymptotic limit as $m_Q \rightarrow \infty$,

$$\Phi_{\text{hl}}(1/m_Q) = \Phi_{\text{hl}}(0) \exp \left[\sum_{p=1}^{\infty} \gamma_p \left(\frac{\Lambda_{\text{QCD}}}{m_Q} \right)^p \right], \quad (4)$$

where m_Q is a heavy quark mass, which is heavier than the QCD scale Λ_{QCD} . Equivalently, the expansion is written as

$$\begin{aligned} \Phi_{\text{hl}}(1/m_Q) &= \Phi_{\text{hl}}(1/m_{Q_A}) \\ &\times \exp \left[\sum_{p=1}^{\infty} \gamma_p \left\{ \left(\frac{\Lambda_{\text{QCD}}}{m_Q} \right)^p - \left(\frac{\Lambda_{\text{QCD}}}{m_{Q_A}} \right)^p \right\} \right], \end{aligned} \quad (5)$$

using some ‘‘anchor’’ point m_{Q_A} . (In Eq. 4 the static limit $m_Q \rightarrow \infty$ is regarded as an anchor point.) Our task is to determine the expansion coefficients γ_p and the overall factor $\Phi_{\text{hl}}(1/m_{Q_A})$ to reach a physical b quark point. There are several ways to the determination:

- (i) HQET approach: The anchor point is static limit $m_Q \rightarrow \infty$. To treat the heavy quark expansion from the static limit, the HQET is employed. In addition to terms in the heavy quark action and operators at the leading order of the expansion (static approximation), those at $O(1/m_Q)$ are included. To keep the theory renormalizable, the Boltzmann factor for the heavy quark is expanded in $1/m_Q$, making operator insertions in the expectation value evaluated with the static action. The HQET must be matched with the original full theory. An important point is that the matching beyond static approximation cannot be carried out perturbatively, because of the existence of $1/a$ power divergence in the HQET [9, 10].
- (ii) Relativistic approach: The anchor point sits in lower mass region, typically c quark mass region.

The usual relativistic formulations can be applicable in that region, while relatively finer lattices are required.

- (iii) Combination of (i) and (ii) above: The anchor point is the static limit, while γ_{ps} are explored by using usual relativistic formulations in lower quark mass region, i.e., c quark region. (For example, Ref. [11].)

Procedure (i) has been used by ALPHA Collaboration, in which nonperturbative matching with QCD full theory can be implemented by the step scaling strategy with Schrödinger functional scheme [10]. (See Ref. [12] for their recent achievements.) In the procedure (ii), relatively finer lattices with regular size of volume are required. However, the lattices to treat c quark are currently becoming available and the approach (ii) is becoming feasible. A recent sophisticated implementation in this direction is “ratio method” [13] by ETM Collaboration, which may be a viable option. In this method, ratios of physical quantities at some heavy quark mass point m_Q and m_Q/λ with a scale parameter $\lambda > 1$, are considered to separate $\Phi_{\text{hl}}(1/m_{Q_A})$ and γ_{ps} in the determination:

$$\frac{\Phi_{\text{hl}}(1/m_Q)}{\Phi_{\text{hl}}(\lambda/m_Q)} = \exp \left[\sum_{p=1}^{\infty} \gamma_p (1 - \lambda^p) \left(\frac{\Lambda_{\text{QCD}}}{m_Q} \right)^p \right], \quad (6)$$

which enhances the precision of the γ_{ps} . (See Ref. [14] for their recent achievements.) A combination of the ratio method and the static limit as an anchor point would also be beneficial, which belongs to the category (iii). In this sense, the static limit is not only of theoretical interest, but also a valuable anchor point to explore physics at physical b quark point. The fact that “the static limit is close to the physical b quark mass in terms of $1/m_Q$ ” ensures usefulness of the static limit as a “strong” anchor point.

III. PHYSICAL OBSERVABLES

A. Observables in QCD full theory

Our main aim in this paper is to calculate the CKM matrix elements V_{td} and V_{ts} to give constraints on the CKM unitary triangle. The current accuracy of the mass difference (1) from experiment is less than 1%, thus precise determination of the hadronic matrix element \mathcal{M}_{B_q} would give strong constraints on the CKM matrix elements. We here summarize current world average values related with neutral B meson mixing, which are quoted

from Particle Data Group (PDG) [15]:

$$m_b(\overline{\text{MS}}) = 4.18 \pm 0.03 \text{ GeV}, \quad (7)$$

$$m_{B^0} = 5279.58 \pm 0.17 \text{ MeV}, \quad (8)$$

$$m_{B_s^0} = 5366.77 \pm 0.24 \text{ MeV}, \quad (9)$$

$$\begin{aligned} \Delta m_{B^0} &= (0.510 \pm 0.004) \times 10^{12} \text{ } \hbar\text{s}^{-1} \\ &= (3.337 \pm 0.033) \times 10^{-10} \text{ MeV}, \end{aligned} \quad (10)$$

$$\begin{aligned} \Delta m_{B_s^0} &= (17.69 \pm 0.08) \times 10^{12} \text{ } \hbar\text{s}^{-1} \\ &= (1.164 \pm 0.005) \times 10^{-8} \text{ MeV}. \end{aligned} \quad (11)$$

Thus, the ratio of the CKM matrix elements (2) reads

$$\left| \frac{V_{td}}{V_{ts}} \right| = \xi \times (0.17071 \pm 0.00092), \quad (12)$$

which indicates the determination of ξ with high accuracy would yield precise value of the ratio.

The $\Delta B = 2$ mixing matrix element at a scale μ_b in the effective Hamiltonian is represented by

$$\begin{aligned} \mathcal{M}_{B_q}(\mu_b) &= \langle \bar{B}_q^0 | [\bar{b}\gamma_\mu(1 - \gamma_5)q][\bar{b}\gamma_\mu(1 - \gamma_5)q] | B_q^0 \rangle_{\text{full}} \\ &\equiv \langle \bar{B}_q^0 | O_L^{\text{full}} | B_q^0 \rangle_{\text{full}}, \end{aligned} \quad (13)$$

where b and q represent b quark and light (d or s) quark fields, respectively. In Eq. (13), we put a superscript and a subscript “full” to indicate that the theory considered here is not HQET, but rather QCD full theory. In this paper, the standard PDG notation for the quark content of B meson is used; $B = (\bar{b}q)$ and $\bar{B} = (b\bar{q})$. The matrix element is conventionally parametrized as

$$\mathcal{M}_{B_q}(\mu_b) = \frac{8}{3} m_{B_q}^2 f_{B_q}^2 B_{B_q}(\mu_b), \quad (14)$$

so that $B_{B_q} = 1$ when vacuum saturation approximation (VSA) exactly holds, where B_{B_q} depicts a dimensionless hadronic B -parameter and f_{B_q} denotes B_q meson decay constant defined by

$$\begin{aligned} i f_{B_q} p_\mu &= \langle 0 | \bar{b}\gamma_\mu \gamma_5 q | B_q(p) \rangle_{\text{full}} \\ &\equiv \langle 0 | A_\mu^{\text{full}} | B_q(p) \rangle_{\text{full}}, \end{aligned} \quad (15)$$

with four-momentum of B_q meson p_μ . An RGI definition of the B -parameters \hat{B}_{B_q} is obtained from B -parameters in some scheme and at some scale μ_b by:

$$\hat{B}_{B_q} = [\alpha_s(\mu_b)]^{-\frac{\gamma_0}{2\beta_0}} \left(1 - \frac{\alpha_s(\mu_b)}{4\pi} Z_5 \right) B_{B_q}(\mu_b), \quad (16)$$

at next-to-leading order (NLO), where Z_5 in naive dimensional regularization (NDR) with the modified minimal subtraction ($\overline{\text{MS}}$) scheme is written as [16]

$$Z_{n_f} = \frac{\gamma^{(1)}}{2\beta_0} - \frac{\gamma^{(0)}\beta_1}{2\beta_0^2}, \quad (17)$$

with

$$\beta_0 = 11 - \frac{2}{3}n_f, \quad \beta_1 = 102 - \frac{38}{3}n_f, \quad (18)$$

$$\gamma^{(0)} = 4, \quad \gamma^{(1)} = -7 + \frac{4}{9}n_f. \quad (19)$$

In this study we use $\alpha_s(\mu_b) = 0.2265$ obtained from strong coupling at Z boson mass scale $\alpha_s(m_Z = 91.1876(21) \text{ GeV}) = 0.1185(6)$ [15] using renormalization group (RG) evolution (four-loop [17, 18]) with $n_f = 5$. Eq. (16) thus becomes $\hat{B}_{B_q} = 1.516 \times B_{B_q}(\mu_b)$.

One of the focal point of this paper is SU(3) breaking ratio (3), which should be unity in the SU(3) light flavor symmetric case. In this ratio most of the theoretical uncertainties as well as statistical fluctuations are largely canceled out. Using the parametrization of the matrix element (14), the SU(3) breaking ratio is represented as

$$\xi = \frac{f_{B_s}}{f_B} \sqrt{\frac{B_{B_s}}{B_B}}. \quad (20)$$

Because B -parameters are based on VSA by definition and there is a suppression factor due to SU(3) light flavor symmetry, the ratio of B -parameters in Eq. (20) could be close to one and a large fraction of the SU(3) breaking of ξ likely to reside in the ratio of B meson decay constants.

B. Observables in static limit

We regard the b quark as a heavy quark and give it an on-shell velocity $v_\mu = (1, 0, 0, 0)$, which leads to an on-shell momentum $p_\mu = (m_b, 0, 0, 0)$. Heavy quark field h is introduced as a sum of heavy quark h_+ and anti-heavy quark h_- :

$$h = h_+ + h_-, \quad \bar{h} = \bar{h}_+ + \bar{h}_- = h_+^\dagger - h_-^\dagger, \quad (21)$$

through

$$h_\pm = e^{\mp i m_b v \cdot x} \frac{1 \pm \not{v}}{2} b = e^{\mp i m_b t} \frac{1 \pm \gamma_0}{2} b, \quad (22)$$

where b is a usual relativistic quark field.

In the static limit, the B meson decay constant and the hadronic matrix element behave like $f_{B_q} \propto 1/\sqrt{m_{B_q}}$ and $\mathcal{M}_{B_q} \propto m_{B_q}$, respectively. Therefore it would be useful to introduce quantities:

$$\Phi_{B_q} = \sqrt{m_{B_q}} f_{B_q}, \quad M_{B_q} = \frac{\mathcal{M}_{B_q}}{m_{B_q}}, \quad (23)$$

so that they behave as constants in the static limit. Hadron states in the HQET are labeled by v_μ and a residual momentum k_μ , which satisfies $v \cdot k = 0$. They are defined in the static limit and differ from those of the QCD full theory:

$$|B_q\rangle_{\text{full}} = \sqrt{m_{B_q}} \{|B_q\rangle_{\text{HQET}} + O(\Lambda_{\text{QCD}}/m_b)\}, \quad (24)$$

so that the HQET state normalization becomes

$$\langle B_q(\vec{k}) | B_q(\vec{k}') \rangle_{\text{HQET}} = 2(2\pi)^3 \delta^3(\vec{k} - \vec{k}'). \quad (25)$$

Using the HQET state, Φ_{B_q} in Eq. (23) is simply written as

$$\begin{aligned} \Phi_{B_q} &= \langle 0 | \bar{h} \gamma_0 \gamma_5 q | B_q \rangle_{\text{HQET}} \\ &\equiv \langle 0 | A_0^{\text{HQET}} | B_q \rangle_{\text{HQET}} \end{aligned} \quad (26)$$

For M_{B_q} , we need two kinds of matrix element:

$$\begin{aligned} M_L &= \langle \bar{B}_q^0 | [\bar{h} \gamma_\mu (1 - \gamma_5) q] [\bar{h} \gamma_\mu (1 - \gamma_5) q] | B_q^0 \rangle_{\text{HQET}} \\ &\equiv \langle \bar{B}_q^0 | O_L^{\text{HQET}} | B_q^0 \rangle_{\text{HQET}}, \end{aligned} \quad (27)$$

$$\begin{aligned} M_S &= \langle \bar{B}_q^0 | [\bar{h} (1 - \gamma_5) q] [\bar{h} (1 - \gamma_5) q] | B_q^0 \rangle_{\text{HQET}} \\ &\equiv \langle \bar{B}_q^0 | O_S^{\text{HQET}} | B_q^0 \rangle_{\text{HQET}}, \end{aligned} \quad (28)$$

owing to lack of four-dimensional Euclidean rotational symmetry in the static limit, where the $\Delta B = 2$ four quark operator O_L is decomposed into spatial and time components:

$$\sum_{i=1,2,3} [\bar{h} \gamma_i (1 - \gamma_5) q] [\bar{h} \gamma_i (1 - \gamma_5) q], \quad (29)$$

$$[\bar{h} \gamma_0 (1 - \gamma_5) q] [\bar{h} \gamma_0 (1 - \gamma_5) q], \quad (30)$$

and they are renormalized differently. As a consequence, operators (27) and (28) have mixings. In the following, B meson states $|B_q\rangle$ and operators represent those in the static limit of b quark unless stated otherwise.

IV. LATTICE ACTIONS AND GLUON ENSEMBLES

A. Lattice action

We perform lattice simulations in HQET side, where lattice action comprises three pieces:

$$S = S_{\text{static}} + S_{\text{DWF}} + S_{\text{gluon}}, \quad (31)$$

where S_{static} is the static quark action representing the heavy (b) quark, S_{DWF} is the domain-wall fermion (DWF) action describing the light (u, d, s) quarks and S_{gluon} is the gluon action.

1. Standard static heavy quark action with link smearing

The standard static quark action [5] is given by

$$\begin{aligned} S_{\text{static}} &= \sum_x \bar{h}(x) \\ &\times \left\{ \frac{1 + \gamma_0}{2} \left[h(x) - U_0^\dagger(x - \hat{0}) h(x - \hat{0}) \right] \right. \\ &\quad \left. - \frac{1 - \gamma_0}{2} \left[U_0(x) h(x + \hat{0}) - h(x) \right] \right\}. \end{aligned} \quad (32)$$

The lattice derivatives used here are not symmetric for each heavy and anti-heavy quark, thus fermion doublers do not arise. The form of the action is technically the same as the Wilson quark action with volume reduction into one dimension (time direction). Therefore it has a Wilson term, which decouples from any low-energy physics in the continuum limit and explicitly breaks the chiral symmetry at finite lattice spacing. This action

suffers from huge $1/a$ power divergences, which results in tremendous noise in correlators. The solution to this problem is to introduce link smearing aiming at a reduction of the power divergences [8]. The modification is simply to replace link variables $U_0(x)$ with 3-step hyper-cubic blocked [19] ones $V_0(x)$, which is defined by

$$V_\mu(x) = \text{Proj}_{\text{SU}(3)} \left[(1 - \alpha_1) U_\mu(x) + \frac{\alpha_1}{6} \sum_{\pm\nu \neq \mu} \tilde{V}_{\nu;\mu}(x) \tilde{V}_{\mu;\nu}(x + \hat{\nu}) \tilde{V}_{\nu;\mu}^\dagger(x + \hat{\mu}) \right], \quad (33)$$

$$\tilde{V}_{\mu;\nu}(x) = \text{Proj}_{\text{SU}(3)} \left[(1 - \alpha_2) U_\mu(x) + \frac{\alpha_2}{4} \sum_{\pm\rho \neq \nu, \mu} \bar{V}_{\rho;\nu\mu}(x) \bar{V}_{\mu;\rho\nu}(x + \hat{\rho}) \bar{V}_{\rho;\nu\mu}^\dagger(x + \hat{\mu}) \right], \quad (34)$$

$$\bar{V}_{\mu;\nu\rho}(x) = \text{Proj}_{\text{SU}(3)} \left[(1 - \alpha_3) U_\mu(x) + \frac{\alpha_3}{2} \sum_{\pm\eta \neq \rho, \nu, \mu} U_\eta(x) U_\mu(x + \hat{\eta}) U_\eta^\dagger(x + \hat{\mu}) \right], \quad (35)$$

where $\text{Proj}_{\text{SU}(3)}$ denotes an $\text{SU}(3)$ projection and $(\alpha_1, \alpha_2, \alpha_3)$ are hyper-cubic blocking parameters [19]. $(\alpha_1, \alpha_2, \alpha_3) = (0, 0, 0)$ corresponds to unsmeared link ($V_\mu = U_\mu$). We use two parameter choices in this work:

$$(\alpha_1, \alpha_2, \alpha_3) = \begin{cases} (0.75, 0.6, 0.3) & : \text{HYP1 [19]} \\ (1.0, 1.0, 0.5) & : \text{HYP2 [8]} \end{cases} \quad (36)$$

2. Domain-wall fermion action

The DWF action [20–22] is described by

$$S_{\text{DWF}} = \sum_{s, s'=1}^{L_s} \sum_{x, y} \bar{\psi}_s(x) D_{ss'}^{\text{DWF}}(x, y) \psi_{s'}(y) - \sum_x m_f \bar{q}(x) q(x), \quad (37)$$

$$D_{ss'}^{\text{DWF}}(x, y) = D^4(x, y) \delta_{ss'} + D^5(s, s') \delta_{xy} + (M_5 - 5) \delta_{ss'} \delta_{xy}, \quad (38)$$

$$D^4(x, y) = \sum_\mu \frac{1}{2} [(1 - \gamma_\mu) U_\mu(x) \delta_{x+\hat{\mu}, y} + (1 + \gamma_\mu) U_\mu^\dagger(y) \delta_{x-\hat{\mu}, y}], \quad (39)$$

$$D^5(s, s') = \begin{cases} P_L \delta_{2, s'} & (s = 1) \\ P_L \delta_{s+1, s'} + P_R \delta_{s-1, s'} & (1 < s < L_s) \\ P_R \delta_{L_s-1, s'} & (s = L_s) \end{cases}, \quad (40)$$

where $\psi_s(x)$ are 4+1-dimensional fermion fields. The fifth dimension extends from 1 to L_s and is labeled by the indices s and s' . The domain-wall height (fifth dimensional mass) M_5 is a parameter of the theory which

can be set between $0 < M_5 < 2$. We use a setting of $M_5 = 1.8$. The physical four-dimensional quark field $q(x)$ is constructed from the fields $\psi_s(x)$ at $s = 1$ and L_s :

$$q(x) = P_L \psi_1(x) + P_R \psi_{L_s}(x), \quad (41)$$

$$\bar{q}(x) = \bar{\psi}_1(x) P_R + \bar{\psi}_{L_s}(x) P_L, \quad (42)$$

where P_L and P_R are left and right chirality projectors: $P_L = (1 - \gamma_5)/2$, $P_R = (1 + \gamma_5)/2$. In infinite L_s limit, the right and left-handed modes are decoupled and chiral symmetry is exactly restored. The presence of the chiral symmetry plays a crucial role for reducing unphysical operator mixing. Note that the DWF is automatically $O(a)$ improved [23].

3. Gluon action

We consider a class of RG-improved gluon actions in this study:

$$S_{\text{gluon}} = -\frac{2}{g_0^2} \left((1 - 8c_1) \sum_P \text{ReTr}[U_P] + c_1 \sum_R \text{ReTr}[U_R] \right), \quad (43)$$

where g_0 denotes the bare lattice coupling, U_P and U_R are the path-ordered product of links along a 1×1 plaquette P and the path-ordered product of links along a 1×2 rectangle R , respectively. Our choice of the parameter c_1 is -0.331 (Iwasaki gluon action) [24, 25].

B. Gluon ensembles

We use 2 + 1 flavor dynamical DWF gluon configurations generated by RBC and UKQCD Collaborations [26]. A summary of the ensembles used in this work is listed in Tab. I. Two lattice spacings $a \sim 0.114$ [fm] and 0.0864 [fm] are used to take a continuum limit. We label the coarser and finer lattices as “24c” and “32c”, respectively, representing their lattice sizes. The physical box size is set to be modest, which is around 2.75 [fm]. The size of the fifth dimension is $L_s = 16$ making the chiral symmetry breaking quite small with residual masses $m_{\text{res}} \simeq 0.003$ and 0.0007 for 24c and 32c, respectively. Degenerate u and d quark mass parameters are chosen so that the simulation covers the pion mass range of 290 – 420 [MeV]. The smallest value of $m_\pi L$ is 4.06 , which implies finite volume effect would be small at simulation points. Only one sea s quark mass parameter is taken in our lattice ensemble for both lattice spacings, which is larger than the physical s quark mass by a small amount. As we will explain in Sec. VII, we basically use $\text{SU}(2)$ chiral perturbation theory fit functions assuming sea s quark mass sits on physical point, while the actual sea s quark mass in this simulation is not physical one. The uncertainty from this inconsistency is estimated by the partially quenched $\text{SU}(3)$ chiral perturbation theory

TABLE I. $2+1$ flavor dynamical domain-wall fermion ensembles by RBC/UKQCD Collaborations.[26] Physical quark masses are obtained using $SU(2)\chi$ PT in the chiral extrapolation. $m_{ud/s}^{\text{phys}} = m_{l/h}^{\text{phys}} + m_{\text{res}}(m_h^{\text{sim}})$.

label	β	$L^3 \times T \times L_s$	a^{-1} [GeV]	a [fm]	aL [fm]	$m_{ud}^{\text{phys}}/m_s^{\text{phys}}$	$m_{\text{res}}(m_h^{\text{phys}})$	$m_{\text{res}}(m_h^{\text{sim}})$	m_l/m_h	$m_\pi(m_h^{\text{phys}})$ [MeV]	$m_\pi L$
24c1	2.13	$24^3 \times 64 \times 16$	1.729(25)	0.114	2.74	0.00134(4)	0.003076(58)	0.003152(43)	0.005/0.04	327	4.54
24c2						/0.0379(11)			0.01/0.04	418	4.79
32c1	2.25	$32^3 \times 64 \times 16$	2.280(28)	0.0864	2.76	0.00100(3)	0.006643(82)	0.0006664(76)	0.004/0.03	289	4.06
32c2						/0.0280(7)			0.006/0.03	344	4.83
32c3									0.008/0.03	393	5.52

as explained in Sec. VIII and turns out to be less than 1%. For a valence s quark, we make measurements with two s quark mass parameters sandwiching the physical s quark mass and make a linear interpolation.

V. MATCHING

In this work, we adopt a two step matching: the first is a matching between QCD full theory and HQET in the continuum, the second is a matching between the continuum and the lattice in HQET. The matching is carried out by one-loop perturbative calculation. Here we summarize key points of the matching.

- The full theory operators in the continuum are renormalized in $\overline{\text{MS}}(\text{NDR})$ scheme at $\mu_b = m_b$, b quark mass scale. Fierz transformations in arbitrary dimensions are specified in the naive dimensional regularization (NDR) scheme by Buras and Weisz evanescent operators [27].
- The HQET operators in the continuum are also renormalized in $\overline{\text{MS}}(\text{NDR})$ scheme at some scale μ .
- Matching operators between full theory and HQET in the continuum is carried out by perturbatively calculating matrix elements of the operators in both theories and comparing them.
- The matching above is performed at scale $\mu = m_b$ to avoid a large logarithm of μ/m_b . We then use renormalization group running in the HQET to go down to a lower scale.
- The HQET operators with the lattice regularization are calculated using a DWF formalism for light quarks to maintain good chiral symmetry, which is important to control the operator mixing.
- Matching HQET operators between continuum and lattice is perturbatively carried out at a lattice cut-off scale $\mu = a^{-1}$, where a denotes a lattice spacing.
- In the perturbative matching, we introduce a fictitious gluon mass to regulate IR divergences. The structure of the IR divergences should be the same

between the continuum and the lattice theories, otherwise they cannot be matched to each other.

- In the matching of HQET operators between continuum and lattice, $O(a)$ discretization errors are taken into account. We employ on-shell $O(a)$ improvement program, in which we impose the equation of motion on the external heavy and light quark lines. In the improvement, we include both $O(pa)$ and $O(ma)$ contributions, where p and m denote light quark momentum and mass, respectively.
- The theory with static approximation of the heavy quark is renormalizable and perturbative renormalization is justified; though this is impossible once $O(1/m_Q)$ correction is included, in which case non-perturbative subtraction of the $1/a$ power divergence is necessary [9, 10]. Inclusion of the $O(a)$ improvement operators does not alter the justification of the perturbative treatment: the $O(a)$ operators just bring $O(\alpha_s^{k+1})$ uncertainty at k th-loop perturbation by mixing with $O(a^0)$ operators, not causing destruction in taking a continuum limit.

In the following, the details are presented.

A. Continuum matching

In the continuum, the QCD full theory and HQET are renormalized at a scale μ , which we specify as a matching point. The operator relation of heavy-light quark bilinear J_Γ and $\Delta B = 2$ four quark operator O_L between the two theories is written as

$$J_\Gamma^{\text{full}}(\mu) = C_\Gamma(\mu) J_\Gamma^{\text{HQET}}(\mu) + O(\Lambda_{\text{QCD}}/m_b), \quad (44)$$

$$O_L^{\text{full}}(\mu) = Z_1(\mu) O_L^{\text{HQET}}(\mu) + Z_2(\mu) O_S^{\text{HQET}}(\mu) + O(\Lambda_{\text{QCD}}/m_b). \quad (45)$$

The one-loop perturbative matching factor for heavy-light axial-vector current is [4]

$$C_{\gamma_0 \gamma_5}(\mu) = 1 + \left(\frac{g}{4\pi}\right)^2 \frac{4}{3} \left[-\frac{3}{2} \ln \left(\frac{\mu^2}{m_b^2} \right) - 2 \right]. \quad (46)$$

For the four quark operator, the one-loop perturbative matching factors are [28, 29]

$$Z_1(\mu) = 1 + \left(\frac{g}{4\pi}\right)^2 \left[-6 \ln\left(\frac{\mu^2}{m_b^2}\right) - 14\right], \quad (47)$$

$$Z_2(\mu) = -8 \left(\frac{g}{4\pi}\right)^2. \quad (48)$$

The numerical values of the matching factors at $\mu = m_b$ are presented in Tab. II.

B. RG running in HQET

To avoid large logarithm of μ/m_b , we match the theories at $\mu = m_b$ in the continuum matching and use RG running to reach a smaller energy scale μ in the HQET side. The running is governed by the RG equation:

$$\mu^2 \frac{d}{d\mu^2} C_\Gamma(\mu) = \frac{1}{2} C_\Gamma(\mu) \gamma_\Gamma, \quad (49)$$

$$\mu^2 \frac{d}{d\mu^2} \begin{bmatrix} Z_1(\mu) & Z_2(\mu) \end{bmatrix} = \frac{1}{2} \begin{bmatrix} Z_1(\mu) & Z_2(\mu) \end{bmatrix} \begin{bmatrix} \gamma_{11} & \gamma_{12} \\ \gamma_{21} & \gamma_{22} \end{bmatrix}, \quad (50)$$

where γ 's are anomalous dimensions. Solutions of the RG equations (49) and (50) are generally written as:

$$C_\Gamma(\mu) = C_\Gamma(\mu') U_\Gamma(\mu', \mu), \quad (51)$$

$$\begin{bmatrix} Z_1(\mu) & Z_2(\mu) \end{bmatrix} = \begin{bmatrix} Z_1(\mu') & Z_2(\mu') \end{bmatrix} \mathbf{U}_L(\mu', \mu), \quad (52)$$

where

$$\mathbf{U}_L(\mu', \mu) = \begin{bmatrix} U_L^{(11)}(\mu', \mu) & U_L^{(12)}(\mu', \mu) \\ U_L^{(21)}(\mu', \mu) & U_L^{(22)}(\mu', \mu) \end{bmatrix}. \quad (53)$$

Note that heavy-quark spin symmetry gives constraints on γ 's:

$$\gamma_{12} = 0, \quad \gamma_{22} = \gamma_{11} + 4\gamma_{21}, \quad (54)$$

which turn into

$$U_L^{(12)}(\mu', \mu) = 0, \quad (55)$$

$$U_L^{(22)}(\mu', \mu) = U_L^{(11)}(\mu', \mu) + 4U_L^{(21)}(\mu', \mu). \quad (56)$$

Each U 's are expressed as

$$U_\Gamma(\mu', \mu) = \left(1 + \frac{\alpha_s(\mu) - \alpha_s(\mu')}{4\pi} J_\Gamma\right) \left[\frac{\alpha_s(\mu')}{\alpha_s(\mu)}\right]^{d_\Gamma} + O(\alpha_s^2), \quad (57)$$

$$U_L^{(11)}(\mu', \mu) = \left(1 + \frac{\alpha_s(\mu) - \alpha_s(\mu')}{4\pi} J_1\right) \left[\frac{\alpha_s(\mu')}{\alpha_s(\mu)}\right]^{d_1} + O(\alpha_s^2), \quad (58)$$

$$U_L^{(21)}(\mu', \mu) = -\frac{1}{4} \left(\left[\frac{\alpha_s(\mu')}{\alpha_s(\mu)}\right]^{d_1} - \left[\frac{\alpha_s(\mu')}{\alpha_s(\mu)}\right]^{d_2} \right) + O(\alpha_s), \quad (59)$$

$$U_L^{(22)}(\mu', \mu) = \left[\frac{\alpha_s(\mu')}{\alpha_s(\mu)}\right]^{d_2} + O(\alpha_s), \quad (60)$$

TABLE II. Numerical values of the one-loop continuum matching factors and RG-running coefficients. [30]

	24c (1.73 GeV)	32c (2.28 GeV)
$\alpha_s(m_b = 4.18 \text{ GeV}[15])$		0.2261
$\alpha_s(m_c = 1.275 \text{ GeV}[15])$		0.3908
$\alpha_s(a^{-1})$	0.3204	0.2773
$C_{\gamma_0 \gamma_5}(m_b)$		0.9520
$U_\Gamma^{N_f=4}(m_b, m_c)$		1.1550
$U_\Gamma^{N_f=3}(m_c, a^{-1})$	0.9521	0.9196
$Z_1(m_b)$		0.7483
$Z_2(m_b)$		-0.1439
$U_L^{(11)N_f=4}(m_b, m_c)$		1.3345
$U_L^{(21)N_f=4}(m_b, m_c)$		-0.0526
$U_L^{(22)N_f=4}(m_b, m_c)$		1.0921
$U_L^{(11)N_f=3}(m_c, a^{-1})$	0.9055	0.8442
$U_L^{(21)N_f=3}(m_c, a^{-1})$	0.0141	0.0231
$U_L^{(22)N_f=3}(m_c, a^{-1})$	0.9706	0.9500

where $\alpha_s = g^2/(4\pi)$. In the one-loop matching, two-loop calculations of the anomalous dimensions and beta-function are required for obtaining J_Γ , d_Γ , J_1 , d_1 and d_2 in Eqs. (57)–(60). The two-loop anomalous dimensions were calculated in Refs. [31, 32] for quark bilinears and in Refs. [29, 33, 34] for four-quark operators.

Because we include sea quarks only for u , d and s in our simulations ($N_f = 2 + 1$) and our lattice cutoff scale is higher than c quark mass, we employ a two-step RG running to reach a scale $\mu = a^{-1}$: making running from $\mu = m_b$ to m_c scale using $N_f = 4$ theory and running back to a^{-1} scale using $N_f = 3$ theory, such as

$$U_\Gamma(m_b, a^{-1}) = U_\Gamma^{N_f=4}(m_b, m_c) U_\Gamma^{N_f=3}(m_c, a^{-1}), \quad (61)$$

$$\mathbf{U}_L(m_b, a^{-1}) = \mathbf{U}_L^{N_f=4}(m_b, m_c) \mathbf{U}_L^{N_f=3}(m_c, a^{-1}), \quad (62)$$

in which

$$d_\Gamma^{N_f=4} = -\frac{6}{25}, \quad d_1^{N_f=4} = -\frac{12}{25}, \quad d_2^{N_f=4} = -\frac{4}{25}, \quad (63)$$

$$J_\Gamma^{N_f=4} = 0.910, \quad J_1^{N_f=4} = 1.864, \quad (64)$$

$$d_\Gamma^{N_f=3} = -\frac{2}{9}, \quad d_1^{N_f=3} = -\frac{4}{9}, \quad d_2^{N_f=3} = -\frac{4}{27}, \quad (65)$$

$$J_\Gamma^{N_f=3} = 0.755, \quad J_1^{N_f=3} = 1.698. \quad (66)$$

The RG-running coefficients are summarized in Tab. II.

C. Static effective theory matching

The matching of the static effective theory between continuum and lattice is carried out at a scale $\mu = a^{-1}$ using one-loop perturbation. In the matching, lattice discretization errors are taken into account up to $O(pa)$ and $O(m_q a)$, where p and m_q are typical light quark momentum and light quark mass, respectively. To include these discretization errors, higher dimensional operators

need to be added in the matching. The operator mixing pattern is constrained by symmetries, typically, chiral symmetry, heavy quark spin symmetry, and discrete symmetries such as \mathcal{P} , \mathcal{T} and \mathcal{C} .

The operator relation for quark bilinear is written as:

$$J_\Gamma^{\text{cont}} = Z_\Gamma J_\Gamma^{\text{imp}}, \quad (67)$$

where J_Γ^{imp} is $O(a)$ improved lattice bilinear:

$$J_\Gamma^{\text{imp}} = J_\Gamma + ac_\Gamma^{(pa)} G J_{\Gamma D} + ac_\Gamma^{(ma)} G J_{\Gamma M}, \quad (68)$$

in which

$$J_{\Gamma D} = \bar{h}\Gamma(\gamma \cdot \vec{D})q, \quad J_{\Gamma M} = m_q \bar{h}\Gamma q, \quad (69)$$

and G is defined by $\gamma_0 \Gamma \gamma_0 = G\Gamma$. For four-quark operators:

$$O_L^{\text{cont}} = Z_L O_L^{\text{imp}}, \quad (70)$$

$$O_S^{\text{cont}} = Z_S O_S^{\text{imp}}, \quad (71)$$

where O_L^{imp} and O_S^{imp} are $O(a)$ improved lattice operators:

$$O_L^{\text{imp}} = O_L + ac_L^{(pa)}(O_{ND} + 2O'_{ND}) + ac_L^{(ma)}(O_{NM} + 2O'_{NM}), \quad (72)$$

$$O_S^{\text{imp}} = O_S + ac_S^{(pa)}(O_{ND} - 2O'_{ND}) + ac_S^{(ma)}(O_{NM} - 2O'_{NM}), \quad (73)$$

with

$$O_{ND} = 2[\bar{h}\gamma_\mu^R(\gamma \cdot \vec{D})q][\bar{h}\gamma_\mu^L q], \quad (74)$$

$$O'_{ND} = 2[\bar{h}P_R(\gamma \cdot \vec{D})q][\bar{h}P_L q], \quad (75)$$

$$O_{NM} = 2m_q[\bar{h}\gamma_\mu^R q][\bar{h}\gamma_\mu^L q], \quad (76)$$

$$O'_{NM} = 2m_q[\bar{h}P_R q][\bar{h}P_L q]. \quad (77)$$

We note that the coefficients for the quark bilinear operator do not depend on Γ , which is a consequence of chiral and heavy quark spin symmetry [30, 35, 36] and this fact holds nonperturbatively. (For the four-quark operators, it is claimed that more higher order operators are required in Eqs. (72) and (73) for the $O(a)$ improvement at higher loop or non-perturbative level [37].)

For the one-loop calculation of coefficients in Eqs. (67), (70) and (71), we use mean-field (MF) improvement to remove huge tad-pole contribution on the lattice perturbation [38]. Measured plaquette value P or $u_0 = P^{1/4}$ comes into the matching for the MF improvement.

We employ DWF as light quarks, thus the physical light quark propagator is written as

$$S_q(p) = \langle q(-p)\bar{q}(p) \rangle = \frac{1 - w_0^2}{i \not{p} + (1 - w_0^2)m_f} (1 + O(p^2, pm_f, m_f^2)), \quad (78)$$

where $w_0 = 1 - M_5$. The physical quark propagator suggests that the quark wave function has a domain-wall specific factor $(1 - w_0^2)^{1/2}$ and the quark mass should be

identified by $m_q = (1 - w_0^2)m_f$, which would appear in the matching coefficients.

The matching coefficients at one-loop level are

$$Z_\Gamma = Z_w^{-1/2} \left\{ 1 + \left(\frac{g_{\overline{\text{MS}}}}{4\pi} \right)^2 \frac{4}{3} \hat{z}_\Gamma^{\text{MF}} \right\} + O(g^4), \quad (79)$$

$$c_\Gamma^{(pa)} = \frac{1}{u_0} \left(\frac{g_{\overline{\text{MS}}}}{4\pi} \right)^2 \frac{4}{3} \hat{z}_\Gamma^{(pa)\text{MF}} + O(g^4), \quad (80)$$

$$c_\Gamma^{(ma)} = \frac{1}{u_0} \left(\frac{g_{\overline{\text{MS}}}}{4\pi} \right)^2 \frac{4}{3} \hat{z}_\Gamma^{(ma)\text{MF}} + O(g^4), \quad (81)$$

$$Z_L = Z_w^{-1} \left\{ 1 + \left(\frac{g_{\overline{\text{MS}}}}{4\pi} \right)^2 \frac{4}{3} \hat{z}_L^{\text{MF}} \right\} + O(g^4), \quad (82)$$

$$c_L^{(pa)} = \frac{1}{u_0} \left(\frac{g_{\overline{\text{MS}}}}{4\pi} \right)^2 \frac{4}{3} \hat{z}_L^{(pa)\text{MF}} + O(g^4), \quad (83)$$

$$c_L^{(ma)} = \frac{1}{u_0} \left(\frac{g_{\overline{\text{MS}}}}{4\pi} \right)^2 \frac{4}{3} \hat{z}_L^{(ma)\text{MF}} + O(g^4), \quad (84)$$

$$Z_S = Z_w^{-1} + O(g^2), \quad (85)$$

$$c_S^{(pa)} = O(g^2), \quad (86)$$

$$c_S^{(ma)} = O(g^2), \quad (87)$$

where

$$Z_w = \frac{1 - (w_0^{\text{MF}})^2}{u_0} \left(1 + \left(\frac{g_{\overline{\text{MS}}}}{4\pi} \right)^2 \frac{4}{3} \hat{z}_w^{\text{MF}} \right) + O(g^4), \quad (88)$$

and the renormalized coupling in the continuum $\overline{\text{MS}}$ scheme $g_{\overline{\text{MS}}}$ at scale $\mu = a^{-1}$ is related to the bare lattice coupling g_0 as:

$$\frac{1}{g_{\overline{\text{MS}}}^2} = \frac{P}{g_0^2} + d_g + c_p + N_f d_f, \quad (89)$$

in which d_g and c_p are dependent on the gluon action and d_f is dependent on the fermion action. Note that the continuum matching coefficient for O_S is already $O(g^2)$, therefore only tree-level static matching coefficient for this operator is needed in the one-loop matching procedure. Nevertheless, we include partly the $O(g^2)$ in Eq. (85) to keep the same form of Z_w as that for Z_L , which does not matter at the one-loop level. The coefficients for this simulation are summarized in Tab. III.

VI. MEASUREMENT AND DATA EXTRACTION

In this section, we present details of measurements on the gluon configurations introduced in Sec. IV.

A. Correlators

In the static limit, energies of states do not depend on their momentum. This fact requires special treatment of correlators, because even in the large separation of source

TABLE III. Numerical values of the one-loop static effective theory matching factors. [30]

	24c		32c	
	HYP1	HYP2	HYP1	HYP2
P (chiral limit)	0.5883		0.6156	
M_5^{MF}	1.3032		1.3432	
$g_{\text{MS}}^2/4\pi$	0.1769		0.1683	
$Z_{\Gamma=\gamma_0\gamma_5}$	0.9105	0.9383	0.9256	0.9526
$c_{\Gamma=\gamma_0\gamma_5}^{(pa)}$	0.0790	0.1374	0.0744	0.1294
$c_{\Gamma=\gamma_0\gamma_5}^{(ma)}$	0.0864	0.1660	0.0739	0.1482
Z_L	0.8260	0.8911	0.8546	0.9187
$c_L^{(pa)}$	0.1185	0.2061	0.1117	0.1942
$c_L^{(ma)}$	0.1296	0.2489	0.1108	0.2222
Z_S	0.9645		1.0040	

and sink positions in time t , unique ground state cannot be obtained [39, 40]. Especially, the Gaussian source and sink smearing used in this work requires taking into account this feature. In this subsection, we follow discussions in Refs. [39, 40] and explicitly show an extension to any form of source and sink smearing function.

We start with defining our state convention. Static action (32) is invariant under spatial local phase rotation of heavy quark fields:

$$h(\vec{x}, t) \longrightarrow e^{i\theta(\vec{x})} h(\vec{x}, t), \quad (90)$$

$$\bar{h}(\vec{x}, t) \longrightarrow e^{-i\theta(\vec{x})} \bar{h}(\vec{x}, t), \quad (91)$$

which leads to Noether's current:

$$J_h(\vec{x}, t) = \bar{h}(\vec{x}, t) h(\vec{x}, t), \quad (92)$$

with a conservation law:

$$\partial_0 J_h(\vec{x}, t) = 0, \quad (93)$$

indicating time-independent charge (heavy quark number density operator) at each spatial point:

$$N_h(\vec{x}) = J_h(\vec{x}, t), \quad (94)$$

which commutes with the Hamiltonian. We can define B meson states in the PDG notation, $B = (\bar{b}q)$ and $\bar{B} = (b\bar{q})$, as eigenstates of $N_h(\vec{x})$,

$$N_h(\vec{y}) |\tilde{B}(\vec{x})\rangle_L = -\delta_{\vec{x}, \vec{y}}^{(3)} |\tilde{B}(\vec{x})\rangle_L, \quad (95)$$

$$\langle \tilde{B}(\vec{x}) | \tilde{B}(\vec{y}) \rangle_L = \delta_{\vec{x}, \vec{y}}^{(3)}, \quad (96)$$

where “ L ” indicates states in the static limit with finite spatial size L . Using these, B meson states with spacial momentum \vec{p} are defined as

$$|B(\vec{p})\rangle_L = \sqrt{2a^3} \sum_{\vec{x}} e^{-i\vec{p}\cdot\vec{x}} |\tilde{B}(\vec{x})\rangle_L, \quad (97)$$

where momentum \vec{p} takes discrete values:

$$\vec{p} = \frac{2\pi}{La} (n_1, n_2, n_3), \quad 0 < n_1, n_2, n_3 \leq L. \quad (98)$$

This state convention gives a normalization

$$\begin{aligned} \langle B(\vec{p}) | B(\vec{q}) \rangle_L &= 2(La)^3 \delta_{\vec{p}, \vec{q}}^{(3)} \\ &\xrightarrow{La \rightarrow \infty} 2(2\pi)^3 \delta^{(3)}(\vec{p} - \vec{q}), \end{aligned} \quad (99)$$

which leads to a relation between finite and infinite volume momentum eigenstates

$$|B(\vec{p})\rangle_L \xrightarrow{La \rightarrow \infty} |B(\vec{p})\rangle, \quad (100)$$

$$\langle B(\vec{p}) | B(\vec{q}) \rangle = 2(2\pi)^3 \delta^{(3)}(\vec{p} - \vec{q}), \quad (101)$$

so that infinite volume static states $|B(\vec{p})\rangle$ give a conventional normalization (101). Thus what we need to calculate in the finite volume are

$$\langle 0 | A_0(\vec{0}, 0) | B(\vec{p} = 0) \rangle_L \xrightarrow{La \rightarrow \infty} \Phi_B, \quad (102)$$

$$\langle B(\vec{p} = 0) | O_{4q}(\vec{0}, 0) | B(\vec{p} = 0) \rangle_L \xrightarrow{La \rightarrow \infty} M_B, \quad (103)$$

where $A_0(\vec{x}, t)$ and $O_{4q}(\vec{x}, t)$ are local heavy-light axial-vector current (in time direction) and four-quark operators defined in Eqs. (26), (27) and (28). The statement mentioned earlier in this subsection that the B meson energy does not depend on its momentum is understandable as the B meson states defined in Eq. (95) are also energy eigenstates, where the energy does not depend on spatial coordinates due to translational invariance of the system, and the energy, as a consequence, is independent of momentum by Eq. (97). This property requires unfamiliar treatment on correlators. A typical example is an operator which includes spatially smeared quark field:

$$\begin{aligned} A_0^S(\vec{x}, t) &= \left(\sum_{\vec{y}} f(\vec{y}) \bar{h}(\vec{x} + \vec{y}, t) \right) \gamma_0 \gamma_5 \\ &\quad \cdot \left(\sum_{\vec{z}} g(\vec{z}) q(\vec{x} + \vec{z}, t) \right), \end{aligned} \quad (104)$$

where $f(\vec{y})$ and $g(\vec{z})$ are smearing functions, such as Gaussian and wall-type. Consider B meson decay amplitude with the smeared operator and take a large t limit:

$$\begin{aligned} &\langle 0 | A_0^S(\vec{x}, t) | B(\vec{p}) \rangle_L \\ &\xrightarrow[t \gg 0]{} e^{i\vec{p}\cdot\vec{x}} e^{-E_0 t} \langle 0 | A_0^S(\vec{0}, 0) | B(\vec{p}) \rangle_L \\ &\neq \delta_{\vec{p}, \vec{0}}^{(3)} e^{-E_0 t} \langle 0 | A_0^S(\vec{0}, 0) | B(\vec{p} = 0) \rangle_L, \end{aligned} \quad (105)$$

where E_0 represents an energy of B meson ground state. Thus we cannot obtain unique zero-momentum state even in the large t limit, because B meson energy does not depend on spatial momentum \vec{p} any more. This fact causes unusual derivation of matrix elements. Let us demonstrate it here. We consider three-point function with smeared quark fields

$$C_{4q}^{SS}(t_f, t, 0) = a^3 \sum_{\vec{x}} \langle A_0^S(\vec{0}, t_f) O_{4q}(\vec{x}, t) A_0^{S\dagger}(\vec{0}, 0) \rangle. \quad (106)$$

Using completeness of states:

$$1 = \frac{1}{2(La)^3} \sum_{\vec{p}} |B(\vec{p})\rangle_L \langle B(\vec{p})| + (\text{higher states}), \quad (107)$$

the three-point function becomes

$$\begin{aligned} \mathcal{C}_{4q}^{SS}(t_f, t, 0) &\xrightarrow[t_f \gg t \gg 0]{} \\ &\frac{1}{4(La)^3} \sum_{\vec{p}} e^{-E_0 t_f} \langle 0 | A_0^S(\vec{0}, 0) | B(\vec{p}) \rangle_L \\ &\cdot \langle B(\vec{p}) | O_{4q}(\vec{0}, 0) | B(\vec{p}) \rangle_L \langle B(\vec{p}) | A_0^{S\dagger}(\vec{0}, 0) | 0 \rangle_L \\ &= \frac{1}{2} \mathcal{C}^{SS}(t_f, 0) M_B, \end{aligned} \quad (108)$$

where

$$\begin{aligned} \mathcal{C}^{SS}(t, 0) &= \langle A_0^S(\vec{0}, t) A_0^{S\dagger}(\vec{0}, 0) \rangle \\ &\xrightarrow[t \gg 0]{} \frac{1}{2(La)^3} e^{-E_0 t} \sum_{\vec{p}} |\langle 0 | A_0^S(\vec{0}, 0) | B(\vec{p}) \rangle_L|^2 \\ &= \mathcal{A}^{SS} e^{-E_0 t}, \end{aligned} \quad (109)$$

and we used

$$\begin{aligned} &\langle B(\vec{p}) | O_{4q}(\vec{0}, 0) | B(\vec{p}) \rangle_L \\ &= \langle B(\vec{p} = 0) | O_{4q}(\vec{0}, 0) | B(\vec{p} = 0) \rangle_L, \end{aligned} \quad (110)$$

following Eq. (97). As seen in Eq. (108), we inevitably have to use $\mathcal{C}^{SS}(t, 0)$, in which sink position is not spatially volume summed, which results in large statistical noise. The matrix element M_B is then obtained as:

$$\mathcal{C}_{4q}^{SS}(t_f, t, 0) \xrightarrow[t_f \gg t \gg 0]{} \mathcal{A}_{4q}, \quad (111)$$

$$M_B = \frac{2\mathcal{A}_{4q}}{\mathcal{A}^{SS} e^{-E_0 t_f}}. \quad (112)$$

To obtain zero-momentum state in two-point functions, we have to use a projection by spatial volume summation of sink operator. What we need to measure for Φ_B are two-point correlation functions:

$$\mathcal{C}^{\bar{L}S}(t, 0) = a^3 \sum_{\vec{x}} \langle A_0(\vec{x}, t) A_0^{S\dagger}(\vec{0}, 0) \rangle, \quad (113)$$

$$\mathcal{C}^{\bar{S}S}(t, 0) = a^3 \sum_{\vec{x}} \langle A_0^S(\vec{x}, t) A_0^{S\dagger}(\vec{0}, 0) \rangle, \quad (114)$$

in which sink operators are volume summed to project into the zero-momentum state, otherwise we cannot obtain the unique state by just taking the large t limit. By inserting completeness of states (107), these two point correlation functions in $t \gg 0$ can be easily written as

$$\begin{aligned} \mathcal{C}^{\bar{L}S}(t, 0) &\xrightarrow[t \gg 0]{} \frac{1}{2} \langle 0 | A_0(\vec{0}, 0) | B(\vec{p} = 0) \rangle_L \\ &\times \langle B(\vec{p} = 0) | A_0^S(\vec{0}, 0) | 0 \rangle_L e^{-E_0 t} \\ &= \mathcal{A}^{\bar{L}S} e^{-E_0 t}, \end{aligned} \quad (115)$$

$$\begin{aligned} \mathcal{C}^{\bar{S}S}(t, 0) &\xrightarrow[t \gg 0]{} \frac{1}{2} |\langle 0 | A_0^S(\vec{0}, 0) | B(\vec{p} = 0) \rangle_L|^2 e^{-E_0 t} \\ &= \mathcal{A}^{\bar{S}S} e^{-E_0 t}. \end{aligned} \quad (116)$$

Φ_B is then obtained through

$$\Phi_B \xrightarrow[t \gg 0]{} \sqrt{2} \frac{\mathcal{C}^{\bar{L}S}(t, 0)}{\sqrt{\mathcal{C}^{\bar{S}S}(t, 0) e^{-E_0 t}}} = \sqrt{2} \frac{\mathcal{A}^{\bar{L}S}}{\sqrt{\mathcal{A}^{\bar{S}S}}}, \quad (117)$$

in which noisy correlator $\mathcal{C}^{SS}(t, 0)$ is not needed in contrast to M_B . In the actual simulation, we use $O(a)$ improved operators to remove $O(a)$ lattice artifact, as indicated in Eqs. (68), (72) and (73) in Sec. V.

B. Source and sink smearing

In an attempt to obtain a better overlap with ground state, we use gauge-invariant Gaussian smearing for source and sink operators. We follow the smearing procedure in Refs. [41, 42]. We choose a Gaussian function with width ω as a smearing function in Eq. (104) for both static and light quarks:

$$f(\vec{x}) = g(\vec{x}) = \exp(-x^2/\omega^2). \quad (118)$$

To achieve this smearing in gauge-invariant way, we use an implementation:

$$\sum_{\vec{y}} f(\vec{y}) \psi(\vec{x} + \vec{y}, t) = \left(1 + \frac{\omega^2}{4N_G} \nabla^2\right)^{N_G} \psi(\vec{x}, t), \quad (119)$$

with the hopping matrix

$$[\nabla^2]_{xy} \equiv \sum_{i=1}^3 \left[U_i(x + \hat{i}) \delta_{x+\hat{i}, y} + U_i^\dagger(x - \hat{i}) \delta_{x-\hat{i}, y} \right], \quad (120)$$

where N_G is the number of times the smearing kernel acts on fermion field $\psi(\vec{x}, t)$, which leads Gaussian function (118) in $N_G \rightarrow \infty$ limit. The choice of parameters ω and N_G is summarized in Tab. IV, which gives physical Gaussian width around 0.45 fm.

C. Measurement parameters

Measurement parameters are summarized in Tab. IV. The valence d quark mass parameter is the same as the degenerate sea u and d quark's. To interpolate to a physical s quark mass, we take two values of s valence quark mass parameters sandwiching the physical point and one of them is set to be the same as sea s quark's. The physical s quark mass is slightly different from the sea s quark mass, so we estimate the uncertainty from this inconsistency by using the partially quenched SU(3) chiral perturbation theory as we describe later.

D. Autocorrelations

The autocorrelation time of the ensemble is investigated using the integrated autocorrelation time for both

TABLE IV. Measurement parameters. N_G and ω are source and sink Gaussian smearing parameters. $\Delta t_{\text{src-sink}}$ represents source-sink separation in three-point functions.

label	m_q	Measured MD traj	# of data	# of src	N_G	ω	$\Delta t_{\text{src-sink}}$
24c1	0.005, 0.034, 0.040	900–8980 every 40	203	4	32	4	20
24c2	0.010, 0.034, 0.040	1460–8540 every 40	178	2			
32c1	0.004, 0.027, 0.030	520–6800 every 20	304	1	40	5	24
32c2	0.006, 0.027, 0.030	1000–7220 every 20	312	1			
32c2	0.008, 0.027, 0.030	520–5540 every 20	252	1			

static heavy-light two-point and three-point functions. The integrated autocorrelation time of two-point functions is measured at $t = 12$ for $\mathcal{C}^{\tilde{L}S}(t, 0)$ and $\mathcal{C}^{\tilde{S}S}(t, 0)$, but at $t = 15$ for $\mathcal{C}^{SS}(t, 0)$ in both 24c and 32c ensemble. We measure it at mid-point between source and sink location for three-point functions. Based on this analysis, we choose to make blocking, so that the blocking size is 80 MD trajectories for 32c1 ensemble (lightest quark mass parameter), whereas 40 MD trajectories for other ensembles. Note that in the study of light hadron spectrum on these ensembles, the blocking size was 20 MD trajectories [26].

E. Correlator fits

In figures in Appendix A, we show effective masses of two-point functions and amplitudes of three-point functions. We perform simultaneous fits of three types of two-point correlators $\mathcal{C}^{\tilde{L}S}(t, 0)$, $\mathcal{C}^{\tilde{S}S}(t, 0)$ and $\mathcal{C}^{SS}(t, 0)$, assuming E_0 is common in these correlators. To take into account the periodicity in the lattice box, a cosh function is assumed in the fit:

$$\mathcal{C}^{\tilde{L}S}(t, 0) = \mathcal{A}^{\tilde{L}S}(e^{-E_0 t} + e^{-E_0(T-t)}), \quad (121)$$

$$\mathcal{C}^{\tilde{S}S}(t, 0) = \mathcal{A}^{\tilde{S}S}(e^{-E_0 t} + e^{-E_0(T-t)}), \quad (122)$$

$$\mathcal{C}^{SS}(t, 0) = \mathcal{A}^{SS}(e^{-E_0 t} + e^{-E_0(T-t)}). \quad (123)$$

For the three-point correlators $\mathcal{C}_L^{SS}(t_f, t, 0)$ and $\mathcal{C}_S^{SS}(t_f, t, 0)$, constant fits are made:

$$\mathcal{C}_L^{SS}(t_f, t, 0) = \mathcal{A}_L^{SS}, \quad (124)$$

$$\mathcal{C}_S^{SS}(t_f, t, 0) = \mathcal{A}_S^{SS}, \quad (125)$$

where t_f is fixed to be source-sink separation shown in Tab. IV. Fit ranges are shown in the effective mass and amplitude plots in Appendix A and the fit results are presented in Tabs. V and VI. Note that the $\mathcal{O}(a)$ -improved $\mathcal{C}_S^{SS}(t_f, t, 0)$ is not calculated, as the one-loop level matching does not require it.

For some quark mass parameters, $\chi^2/\text{d.o.f.}$ exceeds 2. We, however, keep fit ranges unaltered throughout all quark mass parameters, to avoid human bias. Then our correlator fit results have non-negligible fit-range dependence. As we will explain in Sec. VIII, the fit-range dependence are taken into account as an uncertainty of our calculation.

F. Decay constants, matrix elements and B -parameters

The B meson decay constants f_B and mixing matrix elements \mathcal{M}_B are obtained by Eq. (23) through Eqs. (117) and (112). The results obtained are presented in Tab. VII. The statistical error at each simulation point is less than 2% for decay constants while sometimes reaching 5% for matrix elements and B -parameters.

VII. CHIRAL/CONTINUUM EXTRAPOLATION

A. NLO SU(2)HM χ PT formula

Physical quantities at simulated light (u and d) quark mass points are extrapolated to physical degenerate light quark value. In this work, we use next-to-leading order SU(2) heavy-light meson chiral perturbation theory (NLO SU(2)HM χ PT) depicted in Ref. [40]. (See also Ref. [43] for SU(2) χ PT.) In SU(2) χ PT, s quark is integrated out of the theory; effects from s quark are included in low-energy constants (LEC's). The SU(2) χ PT formula is obtained from SU(3) χ PT assuming u and d quark masses are much smaller than s quark mass. The formula does not depend on s quark mass in an explicit way. The convergence of the chiral fit is improved by using the SU(2) χ PT as long as u and d quark masses are sufficiently small [43]. In Ref. [43], it is argued that the RBC/UKQCD DWF ensemble does not show convergence of NLO SU(2) χ PT above the pion mass of 420 MeV for the light hadron masses and decay constants. The ensembles we use in this work stay below that border.

The NLO SU(2) χ PT formula for B_d and B_s quantity (\mathcal{Q}_{B_d} and \mathcal{Q}_{B_s} , respectively) with unitary d quark is gen-

TABLE V. Correlator fit results ($O(a)$ -unimproved).

24c1, $m_h = 0.040$, $m_l = 0.005$											
smear	m_q	E_0	$\mathcal{A}^{\tilde{L}S}$	$\mathcal{A}^{\tilde{S}S}$	\mathcal{A}^{SS}	χ^2/dof	\mathcal{A}_L^{SS}	χ^2/dof	\mathcal{A}_S^{SS}	χ^2/dof	
HYP1	0.005	0.5107(28)	0.1291(33)e+5	0.1386(33)e+10	0.2663(66)e+7	1.3	0.294(13)e+2	0.5	-0.1741(61)e+2	0.5	
	0.034	0.5440(13)	0.1542(18)e+5	0.1512(16)e+10	0.2984(40)e+7	1.5	0.2230(43)e+2	0.6	-0.1357(24)e+2	0.5	
	0.04	0.5510(12)	0.1589(17)e+5	0.1531(15)e+10	0.3038(38)e+7	1.4	0.2064(37)e+2	0.6	-0.1262(21)e+2	0.4	
HYP2	0.005	0.4656(22)	0.1124(23)e+5	0.1407(28)e+10	0.2670(56)e+7	1.2	0.509(15)e+2	0.4	-0.3258(89)e+2	0.2	
	0.034	0.4998(11)	0.1330(13)e+5	0.1543(14)e+10	0.3041(33)e+7	2.1	0.3789(64)e+2	0.4	-0.2412(40)e+2	0.6	
	0.04	0.5073(10)	0.1370(12)e+5	0.1565(13)e+10	0.3099(32)e+7	2.1	0.3487(55)e+2	0.5	-0.2221(35)e+2	0.7	
24c2, $m_h = 0.040$, $m_l = 0.01$											
smear	m_q	E_0	$\mathcal{A}^{\tilde{L}S}$	$\mathcal{A}^{\tilde{S}S}$	\mathcal{A}^{SS}	χ^2/dof	\mathcal{A}_L^{SS}	χ^2/dof	\mathcal{A}_S^{SS}	χ^2/dof	
HYP1	0.01	0.5117(36)	0.1291(42)e+5	0.1368(42)e+10	0.276(10)e+7	1.8	0.299(16)e+2	1.0	-0.1850(81)e+2	1.0	
	0.034	0.5408(22)	0.1493(30)e+5	0.1475(27)e+10	0.3043(69)e+7	1.8	0.2288(73)e+2	1.1	-0.1424(39)e+2	0.5	
	0.04	0.5480(20)	0.1540(28)e+5	0.1494(25)e+10	0.3095(65)e+7	1.8	0.2115(63)e+2	1.2	-0.1322(34)e+2	0.6	
HYP2	0.01	0.4645(30)	0.1094(30)e+5	0.1351(36)e+10	0.2706(83)e+7	0.9	0.547(20)e+2	1.2	-0.344(11)e+2	0.7	
	0.034	0.4955(17)	0.1269(21)e+5	0.1477(23)e+10	0.3002(54)e+7	1.1	0.3986(94)e+2	1.0	-0.2543(62)e+2	0.7	
	0.04	0.5033(16)	0.1309(20)e+5	0.1501(22)e+10	0.3062(52)e+7	1.2	0.3648(82)e+2	1.0	-0.2333(54)e+2	0.7	
32c1, $m_h = 0.030$, $m_l = 0.004$											
smear	m_q	E_0	$\mathcal{A}^{\tilde{L}S}$	$\mathcal{A}^{\tilde{S}S}$	\mathcal{A}^{SS}	χ^2/dof	\mathcal{A}_L^{SS}	χ^2/dof	\mathcal{A}_S^{SS}	χ^2/dof	
HYP1	0.004	0.4231(29)	0.753(19)e+4	0.1195(30)e+10	0.1105(32)e+7	0.4	0.481(44)e+1	0.5	-0.284(21)e+1	0.5	
	0.027	0.4519(14)	0.925(12)e+4	0.1343(16)e+10	0.1262(21)e+7	0.6	0.379(15)e+1	0.7	-0.2264(83)e+1	1.0	
	0.03	0.4557(14)	0.945(12)e+4	0.1355(15)e+10	0.1278(20)e+7	0.7	0.363(14)e+1	0.7	-0.2170(77)e+1	1.1	
HYP2	0.004	0.3816(28)	0.674(16)e+4	0.1198(28)e+10	0.1096(28)e+7	1.0	0.1041(73)e+2	2.0	-0.661(33)e+1	0.1	
	0.027	0.4118(14)	0.832(10)e+4	0.1365(16)e+10	0.1280(19)e+7	1.4	0.802(23)e+1	2.2	-0.496(15)e+1	0.8	
	0.03	0.4157(14)	0.849(10)e+4	0.1379(15)e+10	0.1296(19)e+7	1.5	0.764(21)e+1	2.2	-0.473(13)e+1	0.9	
32c2, $m_h = 0.030$, $m_l = 0.006$											
smear	m_q	E_0	$\mathcal{A}^{\tilde{L}S}$	$\mathcal{A}^{\tilde{S}S}$	\mathcal{A}^{SS}	χ^2/dof	\mathcal{A}_L^{SS}	χ^2/dof	\mathcal{A}_S^{SS}	χ^2/dof	
HYP1	0.006	0.4293(22)	0.809(17)e+4	0.1280(24)e+10	0.1168(26)e+7	0.8	0.480(34)e+1	0.6	-0.297(15)e+1	0.8	
	0.027	0.4530(15)	0.943(13)e+4	0.1381(17)e+10	0.1290(18)e+7	0.9	0.387(12)e+1	0.9	-0.2379(71)e+1	0.4	
	0.03	0.4557(15)	0.957(13)e+4	0.1390(17)e+10	0.1301(18)e+7	1.0	0.374(11)e+1	1.0	-0.2301(67)e+1	0.4	
HYP2	0.006	0.3855(19)	0.708(12)e+4	0.1256(21)e+10	0.1148(22)e+7	0.8	0.1019(48)e+2	0.3	-0.648(26)e+1	0.2	
	0.027	0.4114(14)	0.834(11)e+4	0.1378(17)e+10	0.1288(17)e+7	1.7	0.792(20)e+1	0.5	-0.500(12)e+1	0.3	
	0.03	0.4143(14)	0.846(11)e+4	0.1388(16)e+10	0.1301(16)e+7	1.7	0.764(19)e+1	0.5	-0.483(12)e+1	0.3	
32c3, $m_h = 0.030$, $m_l = 0.008$											
smear	m_q	E_0	$\mathcal{A}^{\tilde{L}S}$	$\mathcal{A}^{\tilde{S}S}$	\mathcal{A}^{SS}	χ^2/dof	\mathcal{A}_L^{SS}	χ^2/dof	\mathcal{A}_S^{SS}	χ^2/dof	
HYP1	0.008	0.4296(24)	0.795(17)e+4	0.1232(24)e+10	0.1135(25)e+7	0.7	0.491(37)e+1	2.1	-0.285(18)e+1	2.6	
	0.027	0.4529(17)	0.924(15)e+4	0.1337(20)e+10	0.1258(21)e+7	0.8	0.378(18)e+1	1.8	-0.2261(95)e+1	1.6	
	0.03	0.4567(17)	0.943(14)e+4	0.1349(19)e+10	0.1275(21)e+7	0.8	0.361(16)e+1	1.8	-0.2164(88)e+1	1.5	
HYP2	0.008	0.3895(23)	0.717(14)e+4	0.1247(22)e+10	0.1141(24)e+7	1.8	0.958(51)e+1	1.2	-0.605(31)e+1	1.6	
	0.027	0.4126(16)	0.827(11)e+4	0.1351(17)e+10	0.1268(19)e+7	1.8	0.739(28)e+1	1.5	-0.465(17)e+1	2.0	
	0.03	0.4164(15)	0.843(11)e+4	0.1363(16)e+10	0.1284(18)e+7	1.8	0.704(25)e+1	1.5	-0.444(16)e+1	1.9	

erally written as

$$\begin{aligned}
\mathcal{Q}_{B_d} = & \mathcal{Q}_0^{\text{SU}(2)} \left(1 + X_Q \frac{Y_Q + Z_Q (g_{B^* B \pi}^{\text{SU}(2)})^2}{(4\pi f^{\text{SU}(2)})^2} \ell(m_{LL}^2) \right. \\
& + C_{Ql}^{\text{SU}(2)} m_{LL}^2 + C_{Qh}^{\text{SU}(2)} (m_{HH}^2 - m_{HH, \text{phys}}^2) \\
& \left. + C_{Qa}^{\text{SU}(2)} a^2 \right), \quad (126)
\end{aligned}$$

$$\begin{aligned}
\mathcal{Q}_{B_s} = & \mathcal{Q}_0^{(s)} \left(1 + C_{Ql}^{(s)} m_{LL}^2 + C_{Qh}^{(s)} (m_{HH}^2 - m_{HH, \text{phys}}^2) \right. \\
& \left. + C_{Qs}^{(s)} (m_{SS}^2 - m_{HH, \text{phys}}^2) + C_{Qa}^{(s)} a^2 \right), \quad (127)
\end{aligned}$$

where

$$\ell(m_{LL}^2) = m_{LL}^2 \ln \left(\frac{m_{LL}^2}{\Lambda_\chi^2} \right), \quad (128)$$

$$m_{LL}^2 = 2B_0^{\text{SU}(2)} (m_l + m_{\text{res}}), \quad (129)$$

$$m_{HH}^2 = 2B_0^{\text{SU}(2)} (m_h + m_{\text{res}}), \quad (130)$$

$$m_{SS}^2 = 2B_0^{\text{SU}(2)} (m_s + m_{\text{res}}), \quad (131)$$

$$m_{HH, \text{phys}}^2 = 2B_0^{\text{SU}(2)} (m_h^{\text{phys}} + m_{\text{res}}), \quad (132)$$

with m_l , m_h and m_s depicting unitary degenerate u and d , sea s and valence s quark mass, respectively. X_Q , Y_Q and Z_Q are constants specific to each physical quan-

TABLE VI. Correlator fit results ($O(a)$ -improved).

24c1, $m_h = 0.040$, $m_l = 0.005$								
smear	m_q	E_0	$\mathcal{A}^{\tilde{L}S}$	$\mathcal{A}^{\tilde{S}S}$	\mathcal{A}^{SS}	χ^2/dof	\mathcal{A}_L^{SS}	χ^2/dof
HYP1	0.005	0.5107(27)	0.1337(34)e+5	0.1387(32)e+10	0.2664(65)e+7	1.3	0.311(13)e+2	0.4
	0.034	0.5440(13)	0.1600(18)e+5	0.1512(15)e+10	0.2984(40)e+7	1.4	0.2372(45)e+2	0.6
	0.04	0.5510(12)	0.1650(17)e+5	0.1531(14)e+10	0.3037(38)e+7	1.4	0.2198(38)e+2	0.6
HYP2	0.005	0.4654(22)	0.1183(24)e+5	0.1405(27)e+10	0.2668(55)e+7	1.3	0.559(16)e+2	0.4
	0.034	0.4997(10)	0.1406(13)e+5	0.1542(14)e+10	0.3041(33)e+7	2.1	0.4187(68)e+2	0.3
	0.04	0.5072(10)	0.1450(13)e+5	0.1564(13)e+10	0.3098(31)e+7	2.2	0.3858(59)e+2	0.3
24c2, $m_h = 0.040$, $m_l = 0.01$								
smear	m_q	E_0	$\mathcal{A}^{\tilde{L}S}$	$\mathcal{A}^{\tilde{S}S}$	\mathcal{A}^{SS}	χ^2/dof	\mathcal{A}_L^{SS}	χ^2/dof
HYP1	0.01	0.5118(35)	0.1339(43)e+5	0.1371(41)e+10	0.276(10)e+7	1.8	0.318(16)e+2	0.9
	0.034	0.5409(21)	0.1552(30)e+5	0.1477(27)e+10	0.3046(68)e+7	1.8	0.2438(76)e+2	1.1
	0.04	0.5481(19)	0.1601(28)e+5	0.1496(25)e+10	0.3098(64)e+7	1.8	0.2255(66)e+2	1.1
HYP2	0.01	0.4647(29)	0.1155(31)e+5	0.1354(35)e+10	0.2710(81)e+7	0.9	0.600(21)e+2	1.1
	0.034	0.4956(17)	0.1344(21)e+5	0.1479(22)e+10	0.3003(53)e+7	1.1	0.439(10)e+2	0.9
	0.04	0.5034(15)	0.1388(21)e+5	0.1503(21)e+10	0.3063(50)e+7	1.1	0.4028(90)e+2	0.9
32c1, $m_h = 0.030$, $m_l = 0.004$								
smear	m_q	E_0	$\mathcal{A}^{\tilde{L}S}$	$\mathcal{A}^{\tilde{S}S}$	\mathcal{A}^{SS}	χ^2/dof	\mathcal{A}_L^{SS}	χ^2/dof
HYP1	0.004	0.4232(28)	0.775(19)e+4	0.1197(29)e+10	0.1107(31)e+7	0.4	0.505(45)e+1	0.5
	0.027	0.4519(14)	0.953(12)e+4	0.1342(16)e+10	0.1263(21)e+7	0.6	0.399(16)e+1	0.9
	0.03	0.4557(14)	0.973(12)e+4	0.1355(15)e+10	0.1279(21)e+7	0.7	0.382(14)e+1	1.0
HYP2	0.004	0.3818(28)	0.704(17)e+4	0.1200(27)e+10	0.1098(28)e+7	1.0	0.1131(76)e+2	2.0
	0.027	0.4116(14)	0.869(10)e+4	0.1363(15)e+10	0.1278(19)e+7	1.4	0.867(23)e+1	2.3
	0.03	0.4155(13)	0.887(10)e+4	0.1377(15)e+10	0.1295(19)e+7	1.4	0.826(21)e+1	2.3
32c2, $m_h = 0.030$, $m_l = 0.006$								
smear	m_q	E_0	$\mathcal{A}^{\tilde{L}S}$	$\mathcal{A}^{\tilde{S}S}$	\mathcal{A}^{SS}	χ^2/dof	\mathcal{A}_L^{SS}	χ^2/dof
HYP1	0.006	0.4291(21)	0.830(17)e+4	0.1277(24)e+10	0.1166(26)e+7	0.8	0.506(35)e+1	0.7
	0.027	0.4528(15)	0.969(14)e+4	0.1379(17)e+10	0.1288(18)e+7	0.9	0.409(13)e+1	1.2
	0.03	0.4556(14)	0.984(13)e+4	0.1387(16)e+10	0.1299(17)e+7	1.0	0.396(12)e+1	1.3
HYP2	0.006	0.3853(18)	0.737(13)e+4	0.1253(20)e+10	0.1147(22)e+7	0.8	0.1114(50)e+2	0.4
	0.027	0.4113(14)	0.871(12)e+4	0.1376(16)e+10	0.1288(16)e+7	1.8	0.860(22)e+1	0.5
	0.03	0.4142(14)	0.884(12)e+4	0.1386(16)e+10	0.1301(16)e+7	1.8	0.830(20)e+1	0.5
32c3, $m_h = 0.030$, $m_l = 0.008$								
smear	m_q	E_0	$\mathcal{A}^{\tilde{L}S}$	$\mathcal{A}^{\tilde{S}S}$	\mathcal{A}^{SS}	χ^2/dof	\mathcal{A}_L^{SS}	χ^2/dof
HYP1	0.008	0.4296(23)	0.818(17)e+4	0.1233(24)e+10	0.1135(25)e+7	0.7	0.513(37)e+1	1.9
	0.027	0.4529(17)	0.952(15)e+4	0.1338(19)e+10	0.1259(21)e+7	0.8	0.399(18)e+1	1.6
	0.03	0.4567(16)	0.972(15)e+4	0.1350(19)e+10	0.1275(20)e+7	0.8	0.381(17)e+1	1.6
HYP2	0.008	0.3895(22)	0.748(14)e+4	0.1247(21)e+10	0.1142(23)e+7	1.7	0.1035(53)e+2	1.3
	0.027	0.4127(15)	0.865(12)e+4	0.1351(16)e+10	0.1269(19)e+7	1.7	0.804(29)e+1	1.5
	0.03	0.4164(15)	0.882(11)e+4	0.1364(16)e+10	0.1285(18)e+7	1.7	0.766(27)e+1	1.5

tity, given in Tab. VIII. $f^{\text{SU}(2)}$, $B_0^{\text{SU}(2)}$, $g_{B^*B\pi}^{\text{SU}(2)}$, $Q_0^{\text{SU}(2)}$, $C_{Ql}^{\text{SU}(2)}$, $C_{Qh}^{\text{SU}(2)}$, $C_{Qa}^{\text{SU}(2)}$, $Q_0^{(s)}$, $C_{Ql}^{(s)}$, $C_{Qh}^{(s)}$, $C_{Qs}^{(s)}$ and $C_{Qa}^{(s)}$ are LEC's. Note that these LEC's are specific to the $\text{SU}(2)\chi\text{PT}$, in which the effects of s quark are integrated out at a physical s quark mass m_h^{phys} . The s quark mass dependence needs to be included, unless the s quark mass has a physical value. It can be implemented by Taylor expansion of LEC's around the physical s quark mass as shown in Eqs. (126) and (127). In this work, we use two kinds of link smearing in the static quark action. Only coefficients in front of a^2 are dependent on the smearing. We here mention that because the B -parameters express how the VSA holds well, its quark mass dependence is expected to be mild. In fact, the logarithm in the χPT

formula for B_B is suppressed for $g_{B^*B\pi} = 0.449$ [44] used in this study, which leads to smaller coefficient of the logarithm term compared to that of the decay constant and matrix element. For the $\text{SU}(3)$ breaking ratios, the expression up to NLO becomes

$$\begin{aligned}
\frac{Q_{Bs}}{Q_{Ba}} = & \tilde{Q}_0^{\text{SU}(2)} \left(1 - X_Q \frac{Y_Q + Z_Q (g_{B^*B\pi}^{\text{SU}(2)})^2}{(4\pi f^{\text{SU}(2)})^2} \ell(m_{LL}^2) \right. \\
& + \tilde{C}_{Ql}^{\text{SU}(2)} m_{LL}^2 + \tilde{C}_{Qh}^{\text{SU}(2)} (m_{HH}^2 - m_{HH, \text{phys}}^2) \\
& \left. + C_{Qs}^{(s)} (m_{SS}^2 - m_{HH, \text{phys}}^2) + \tilde{C}_{Qa}^{\text{SU}(2)} a^2 \right). \tag{133}
\end{aligned}$$

Note that these expressions do not give unity even at

TABLE VII. Decay constants, matrix elements and B -parameters in lattice unit at simulation points. Φ_{B_s} , Φ_{B_s}/Φ_B , M_{B_s} , $(M_{B_s}/M_B)^{1/2}$, B_{B_s} and $(B_{B_s}/B_B)^{1/2}$ are interpolated to physical s quark mass. Matching factors are multiplied.

HYP1, $O(a)$ -unimproved										
vol	m_l	Φ_B	Φ_{B_s}	Φ_{B_s}/Φ_B	M_B	M_{B_s}	$(M_{B_s}/M_B)^{1/2}$	B_B	B_{B_s}	$(B_{B_s}/B_B)^{1/2}$
24c	0.005	0.2613(38)	0.2998(21)	1.147(12)	0.1580(86)	0.2098(56)	1.152(22)	0.867(38)	0.875(17)	1.004(15)
24c	0.01	0.2630(48)	0.2940(33)	1.118(11)	0.158(10)	0.1986(74)	1.118(20)	0.861(42)	0.861(23)	1.000(15)
32c	0.004	0.1611(22)	0.1872(15)	1.162(12)	0.568(49)	0.788(29)	1.178(42)	0.820(67)	0.843(28)	1.014(34)
32c	0.006	0.1674(20)	0.1880(16)	1.1230(71)	0.625(44)	0.808(30)	1.136(28)	0.837(56)	0.857(26)	1.012(24)
32c	0.008	0.1676(20)	0.1873(17)	1.1179(73)	0.658(49)	0.806(38)	1.107(25)	0.879(59)	0.861(35)	0.990(19)
HYP2, $O(a)$ -unimproved										
vol	m_l	Φ_B	Φ_{B_s}	Φ_{B_s}/Φ_B	M_B	M_{B_s}	$(M_{B_s}/M_B)^{1/2}$	B_B	B_{B_s}	$(B_{B_s}/B_B)^{1/2}$
24c	0.005	0.2327(27)	0.2638(15)	1.134(10)	0.1193(49)	0.1555(34)	1.142(17)	0.825(26)	0.837(14)	1.007(11)
24c	0.01	0.2312(35)	0.2573(23)	1.113(10)	0.1237(57)	0.1521(44)	1.109(14)	0.867(30)	0.861(18)	0.996(10)
32c	0.004	0.1483(20)	0.1718(12)	1.158(11)	0.491(33)	0.670(23)	1.168(32)	0.837(51)	0.851(24)	1.008(25)
32c	0.006	0.1522(15)	0.1713(14)	1.1256(69)	0.505(24)	0.652(20)	1.136(18)	0.817(35)	0.833(20)	1.010(15)
32c	0.008	0.1547(18)	0.1716(14)	1.1093(72)	0.525(25)	0.637(21)	1.102(16)	0.822(35)	0.811(23)	0.993(11)
HYP1, $O(a)$ -improved										
vol	m_l	Φ_B	Φ_{B_s}	Φ_{B_s}/Φ_B	M_B	M_{B_s}	$(M_{B_s}/M_B)^{1/2}$	B_B	B_{B_s}	$(B_{B_s}/B_B)^{1/2}$
24c	0.005	0.2706(38)	0.3112(21)	1.150(12)	0.1661(89)	0.2217(58)	1.156(22)	0.850(36)	0.858(17)	1.005(15)
24c	0.01	0.2726(49)	0.3053(34)	1.120(11)	0.167(10)	0.2105(77)	1.120(20)	0.846(40)	0.846(22)	1.000(14)
32c	0.004	0.1658(22)	0.1928(15)	1.163(12)	0.593(50)	0.824(30)	1.178(41)	0.809(65)	0.831(28)	1.013(33)
32c	0.006	0.1720(20)	0.1935(17)	1.1252(71)	0.654(44)	0.847(31)	1.138(28)	0.829(54)	0.848(25)	1.011(23)
32c	0.008	0.1724(21)	0.1930(17)	1.1196(72)	0.686(49)	0.845(39)	1.110(24)	0.865(57)	0.850(34)	0.991(18)
HYP2, $O(a)$ -improved										
vol	m_l	Φ_B	Φ_{B_s}	Φ_{B_s}/Φ_B	M_B	M_{B_s}	$(M_{B_s}/M_B)^{1/2}$	B_B	B_{B_s}	$(B_{B_s}/B_B)^{1/2}$
24c	0.005	0.2450(28)	0.2791(15)	1.139(10)	0.1295(52)	0.1699(37)	1.145(17)	0.809(25)	0.818(13)	1.006(10)
24c	0.01	0.2439(36)	0.2724(24)	1.1166(98)	0.1348(61)	0.1664(47)	1.111(13)	0.849(28)	0.840(17)	0.9950(96)
32c	0.004	0.1547(20)	0.1795(13)	1.160(11)	0.530(34)	0.717(24)	1.163(31)	0.830(48)	0.834(23)	1.002(23)
32c	0.006	0.1585(16)	0.1790(15)	1.1292(69)	0.545(25)	0.701(21)	1.134(17)	0.813(33)	0.820(19)	1.004(14)
32c	0.008	0.1614(18)	0.1796(15)	1.1124(72)	0.562(27)	0.687(23)	1.106(16)	0.809(34)	0.799(22)	0.994(11)

TABLE VIII. Constants X_Q , Y_Q and Z_Q in Eqs. (126) and (133).

Q	X_Q	Y_Q	Z_Q
Φ	-3/4	1	3
M	-1	2	3
B	-1/2	1	-3

TABLE IX. Low-energy constants used in this work.

LEC's	NLO SU(2) χ PT	NLO SU(2) χ PT(FV)
$B_0^{\text{SU}(2)}$ [GeV] [26]	4.12(7)	4.03(7)
$f^{\text{SU}(2)}$ [GeV] [26]	0.110(2)	0.112(2)
$g_{B^*B\pi}^{\text{SU}(2)}$ [44]	0.449(47) _{stat} (19) _{sys}	
Λ_χ [GeV]	1.0	

$m_l = m_s$ point, because SU(3) flavor symmetry is lost, and SU(2) χ PT formula can be applied only for the region of $m_l \ll m_s$.

B. Details of the chiral fitting

For the chiral fit, we use the values of $f^{\text{SU}(2)}$ and $B_0^{\text{SU}(2)}$ from Ref. [26], of $g_{B^*B\pi}^{\text{SU}(2)}$ from Ref. [44], which are summarized in Tab. IX.

We carry out combined fits using HYP1 and HYP2 link smearing data assuming that terms unrelated to the lattice spacing are common among the smearings. Their correlation is taken into account. As mentioned in the previous subsection, we introduce s quark mass dependence up to linear term. To fully track the sea s quark

dependence, however, at least three independent data in the (m_h, a) parameter space are required. Our simulation setting has only one sea s quark mass parameter for each lattice spacings and the parameter is not tuned to be physical one, therefore the data cannot be fitted using the formula (126), (127) and (133). Nevertheless, we use those formula assuming sea s quark mass parameter is on physical point, leading to sea s quark terms being vanished. Later on we estimate the uncertainty from this inconsistency using partially quenched SU(3) χ PT. On the other hand, we have two valence s quark mass data. In our analysis we first linearly interpolate the data to physical s quark mass point using the two valence data, then the fit functions are applied setting $m_s = m_h^{\text{phys}}$.

In order to take into account ambiguity of the chiral

fit function ansatz, we also use a linear fit function form:

$$\mathcal{G}(m_L, a) = \mathcal{G}_0 (1 + C'_l m_{LL}^2 + C'_a a^2), \quad (134)$$

for B_d quantities and SU(3) breaking ratios, which has the same form as that for B_s sector in SU(2) χ PT framework. We also investigate the uncertainty from chiral fits by eliminating the heaviest quark mass data in both of 24c and 32c ensembles.

C. Scaling check and $O(a)$ improvement

We present fit results using SU(2) χ PT formula in Tab. X. We also show chiral fit using the SU(2) χ PT formula in Figs. 1 and 2, in which both $O(a)$ -unimproved and -improved results are presented. The features of the data are as follows:

- The data shows HYP1 smearing gives larger scaling violations than HYP2.
- HYP1 and HYP2 results are almost consistent with each other in the continuum limit. This consistency is seen even in the $O(a)$ -unimproved case within large statistical errors. While the $O(a)$ -improved data shows slightly better consistency than unimproved one, we cannot see clear effectiveness of the $O(a)$ -improvement at current statistics.
- The $O(a)$ -improvement slightly pushes data up for decay constants and matrix elements at each simulation point.
- Being a ratio, the scaling violation for ξ and f_{B_s}/f_B is tiny. HYP1 and HYP2, $O(a)$ -improved and unimproved results are consistent at each simulation points.

When $O(a)$ -improvement is successfully accomplished and a^2 scaling is used in the continuum extrapolation (assuming $O(\alpha_s^2 a)$ and $O(a^3)$ contributions are small), HYP1 and HYP2 results must give the same value in the continuum limit, and our data is actually consistent with this observation. Therefore we use combined fit of HYP1 and HYP2 assuming chiral fit parameter for each smearing is different only for the coefficients of a^2 term.

D. Fit results and criteria for final results

In this work, $O(a)$ -improved data are taken for the final results. Hereafter, numerical data and figures indicate the $O(a)$ -improved one. We present chiral fit results in Figs. 3, 4 and 5. Correlations between two kinds of link smearing in the static action is included in the fitting. $\chi^2/\text{d.o.f.}$'s and p -values in the fits are presented in the figures. $\chi^2/\text{d.o.f.}$ in each fit are all acceptable level, thus it is hard to exclude any of the fit at the ansatz. We thus take following criteria for the chiral and continuum extrapolations:

- For B_d quantities and SU(3) breaking ratios, an average of results from SU(2) χ PT and the linear fit, whose physical point values are presented in Table XI, is taken. We then take half of the full difference between the SU(2) χ PT and the linear results as an uncertainty from chiral fit function ansatz.
- For B_s quantities, SU(2) χ PT fit (linear fit) results are taken as central values. To investigate the chiral fit form ambiguity, data in region of $m_\pi > 350$ MeV are removed and we see its effect to the extrapolated value. We take difference between the full data and cut data, where the heaviest quark mass points at each lattice spacing are removed (“SU(2) χ PT cut” in Figs. 3, 4 and 5), as a chiral fit ambiguity.

Combining with the ratio of the decay constants, ξ can be obtained through Eq. (20). While the ratio of the B -parameters is well determined, current data for the decay constants has a large uncertainty from chiral extrapolation, which also leads to a poor determination of ξ from Eq. (20), not giving any gain. We hence simply use Eq. (3) to calculate ξ in this work.

E. Finite volume effect

Our lattice has modest physical volume around 2.75 fm and the lowest $m_\pi L$ is about 4, thus we may estimate finite volume (FV) uncertainty using FV NLO χ PT. The FV correction can be included in the χ PT formula by replacing chiral logarithms (128) with [45, 46]

$$\ell(m_{LL}^2) = m_{LL}^2 \ln \left(\frac{m_{LL}^2}{\Lambda_\chi^2} + \delta_1(m_{LL}L) \right), \quad (135)$$

$$\delta_1(m_{LL}L) = \frac{4}{m_{LL}L} \sum_{\vec{r} \neq 0} \frac{K_1(|r|m_{LL}L)}{|r|}, \quad (136)$$

where K_1 is modified Bessel functions of the 2nd kind. For the numerical implementation of Eq. (136), we use the multiplicities depicted in Refs. [43, 45]. With SU(2) χ PT for the chiral extrapolation, we cannot evaluate the FV effect for B_s sector in this procedure. The effect is, however, expected to be quite small in this sector, we estimate this uncertainty is negligible. In the simulated quark mass region, the FV correction slightly pushes the data up for B_d quantities, and hence down for the SU(3) breaking ratios, f_{B_s}/f_B and ξ .

VIII. SYSTEMATIC ERRORS

In this section we clarify the systematic errors we take into account. A summary of the systematic errors is shown in Tab. XII and also in Fig. 6.

TABLE X. Chiral fit results in lattice unit using $SU(2)\chi PT$ formula. The values show physical point and continuum limit results. Matching factors are multiplied.

	HYP1				HYP2				combined			
	$O(a)$ -unimp value	χ^2/dof	$O(a)$ -imp value	χ^2/dof	$O(a)$ -unimp value	χ^2/dof	$O(a)$ -imp value	χ^2/dof	$O(a)$ -unimp value	χ^2/dof	$O(a)$ -imp value	χ^2/dof
Φ_B	0.1437(50)	0.78	0.1460(50)	0.67	0.1400(41)	1.17	0.1436(42)	1.06	0.1392(41)	2.00	0.1428(42)	1.51
Φ_{B_s}	0.1766(37)	0.77	0.1795(38)	0.75	0.1725(30)	1.27	0.1771(31)	1.36	0.1726(31)	2.18	0.1772(32)	1.30
Φ_{B_s}/Φ_B	1.228(23)	0.74	1.229(22)	0.66	1.236(20)	0.33	1.238(20)	0.22	1.233(20)	0.74	1.235(20)	0.69
M_B	0.432(91)	0.37	0.443(93)	0.34	0.410(50)	0.03	0.435(52)	0.01	0.402(50)	0.36	0.430(54)	0.33
M_{B_s}	0.686(64)	0.68	0.704(67)	0.70	0.653(40)	0.09	0.683(43)	0.04	0.636(39)	1.03	0.669(41)	0.86
$\sqrt{M_{B_s}/M_B}$	1.261(62)	0.07	1.261(61)	0.05	1.262(42)	0.19	1.255(41)	0.06	1.262(43)	0.08	1.255(42)	0.04
B_B	0.79(11)	0.20	0.79(11)	0.17	0.753(74)	0.34	0.763(70)	0.42	0.757(78)	0.57	0.766(75)	0.62
B_{B_s}	0.833(53)	0.20	0.829(52)	0.22	0.807(40)	1.23	0.802(38)	1.09	0.804(41)	1.56	0.802(39)	1.45
$\sqrt{B_{B_s}/B_B}$	1.019(45)	0.19	1.020(44)	0.15	1.025(30)	0.13	1.018(29)	0.05	1.023(31)	0.09	1.016(29)	0.09

TABLE XI. Chiral fit results in lattice unit using linear fit function. The values show physical point and continuum limit results. Matching factors are multiplied.

	HYP1				HYP2				combined			
	$O(a)$ -unimp value	χ^2/dof	$O(a)$ -imp value	χ^2/dof	$O(a)$ -unimp value	χ^2/dof	$O(a)$ -imp value	χ^2/dof	$O(a)$ -unimp value	χ^2/dof	$O(a)$ -imp value	χ^2/dof
Φ_B	0.1500(53)	1.17	0.1523(54)	1.03	0.1463(44)	1.63	0.1501(46)	1.48	0.1455(44)	2.14	0.1492(45)	1.63
Φ_{B_s}	0.1766(37)	0.77	0.1795(38)	0.75	0.1725(30)	1.27	0.1771(31)	1.36	0.1726(31)	2.18	0.1772(32)	1.30
Φ_{B_s}/Φ_B	1.164(22)	1.37	1.165(21)	1.27	1.172(20)	1.01	1.174(19)	0.82	1.169(20)	1.00	1.171(19)	0.94
M_B	0.47(10)	0.44	0.48(10)	0.41	0.450(55)	0.03	0.477(58)	0.01	0.442(56)	0.36	0.472(60)	0.32
M_{B_s}	0.686(64)	0.68	0.704(67)	0.70	0.653(40)	0.09	0.683(43)	0.04	0.636(39)	1.03	0.669(41)	0.86
$\sqrt{M_{B_s}/M_B}$	1.186(58)	0.16	1.187(57)	0.13	1.186(40)	0.29	1.180(38)	0.12	1.187(40)	0.12	1.180(39)	0.06
B_B	0.80(11)	0.20	0.80(11)	0.17	0.760(75)	0.33	0.769(71)	0.41	0.763(79)	0.57	0.773(75)	0.61
B_{B_s}	0.833(53)	0.20	0.829(52)	0.22	0.807(40)	1.23	0.802(38)	1.09	0.804(41)	1.56	0.802(39)	1.45
$\sqrt{B_{B_s}/B_B}$	1.015(45)	0.19	1.015(44)	0.15	1.020(30)	0.13	1.013(28)	0.05	1.019(30)	0.09	1.012(29)	0.09

A. Chiral extrapolation

As described in Sec. VII, we use $SU(2)\chi PT$ formula for the chiral and continuum extrapolations. The linear fit function ansatz cannot be excluded in the current statistics, thus we take their average. The method to estimate the associated systematic errors has been described in detail in Sec. VII.

B. $g_{B^*B\pi}$

In the chiral fit, we use $g_{B^*B\pi} = 0.449(47)(19)$, where the first uncertainty is statistical and the second is systematic [44]. This value was obtained using the 2 + 1 flavor dynamical DWF configurations, which is the same as that we use in this simulation. The systematic errors are fully evaluated in Ref. [44], thus we quote this value as a reliable one. We use 0.449 as a central value and change it by ± 0.051 in the chiral fit for the uncertainty of this coupling.

C. Discretization

The static heavy and light quark system has $O(a)$ lattice discretization errors even if chiral fermions are employed for the light quarks, in which case the $O(a)$ discretization errors start with $O(\alpha_s a)$. In this simulation, $O(a)$ -improvement is made using one-loop perturbation theory [30]. Thus, the remaining $O(a)$ lattice artifact is supposed to be $O(\alpha_s^2 a)$ at each simulated lattice spacing a . For the lattice artifact, the coupling should be the lattice one, i.e., defined by Eq. (89), whose actual value is shown in Tab. III. Conservatively assuming $\Lambda_{QCD} \sim 500$ MeV, the order of magnitude for each discretization error is summarized in Tab. XIII. While without one-loop perturbative $O(a)$ -improvement, the magnitude of $O(\alpha_s a)$ term is more than half of $O(a^2)$ term, the improvement makes a substantial reduction of it. The uncertainty from $O(\alpha_s^2 a)$ is $\sim 0.9\%$ (24c) and $\sim 0.6\%$ (32c) level. The uncertainty from $O(a^3)$ contribution, which starts at one-loop level, is even smaller than that. Thus we take 1% as an uncertainty from remaining $O(a)$ and $O(a^3)$ contribution in the continuum. For $SU(3)$ breaking ratios, the lattice artifact comes with a factor of $(m_s - m_d)/\Lambda_{QCD} \sim 0.2$, which leads to reduced uncertainty down to 0.2%.

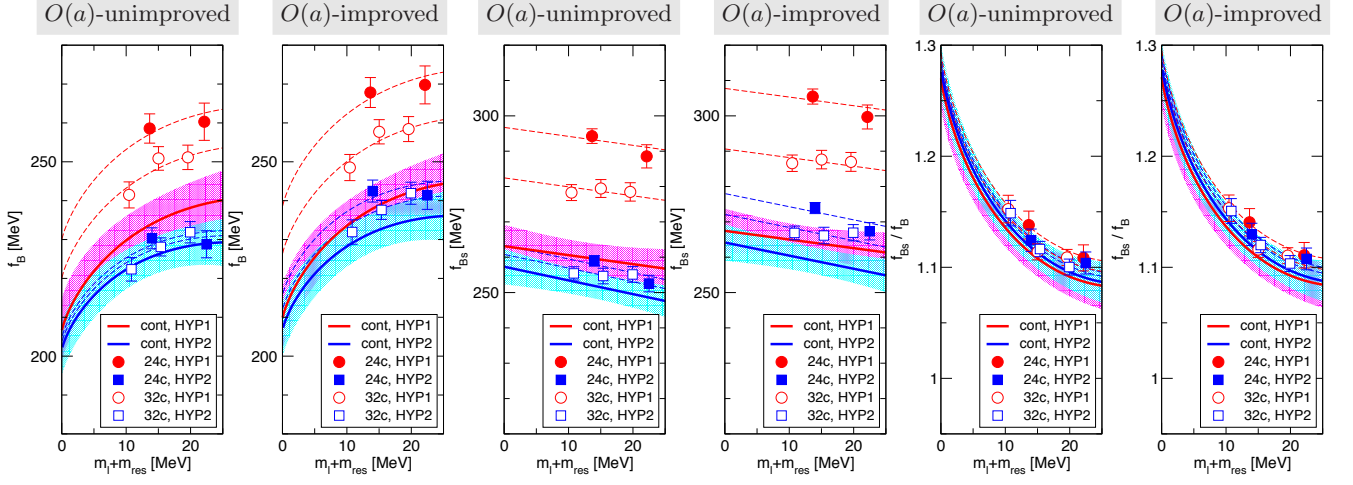


FIG. 1. SU(2)χPT fit of f_B , f_{B_s} and f_{B_s}/f_B comparing $O(a)$ -unimproved and -improved data. HYP1 and HYP2 data are fit independently. Thick lines with band represent continuum limit.

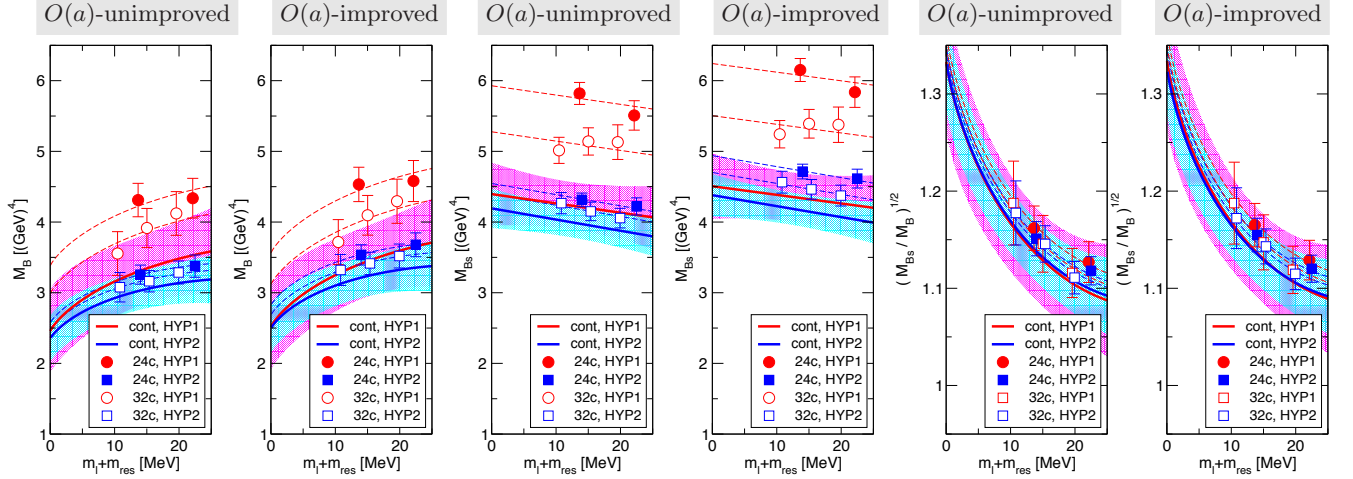


FIG. 2. SU(2)χPT fit of M_B , M_{B_s} and $\sqrt{M_{B_s}/M_B}$ comparing $O(a)$ -unimproved and -improved data. HYP1 and HYP2 data are fit independently. Thick lines with band represent continuum limit.

TABLE XII. Error budget [%] for final quantities.

	f_B	f_{B_s}	f_{B_s}/f_B	$f_B\sqrt{\hat{B}_B}$	$f_{B_s}\sqrt{\hat{B}_{B_s}}$	ξ	\hat{B}_B	\hat{B}_{B_s}	B_{B_s}/B_B
Statistics	2.99	1.81	1.65	6.34	3.12	3.36	9.80	4.93	5.80
Chiral/continuum extrapolation	3.54	1.98	2.66	2.55	2.13	3.08	14.84	7.15	3.66
Finite volume effect	0.82	0.0	1.00	0.76	0.00	1.07	0.15	0.0	0.16
Discretization	1.0	1.0	0.2	1.0	1.0	0.2	1.0	1.0	0.2
One-loop renormalization	6.0	6.0	0.0	6.0	6.0	1.2	6.0	6.0	1.2
$g_{B^*B\pi}$	0.24	0.00	0.35	0.14	0.00	0.25	0.20	0.00	0.22
Scale	1.82	1.85	0.04	1.84	1.86	0.05	0.04	0.05	0.02
Physical quark mass	0.05	0.01	0.06	0.06	0.19	0.20	0.03	0.00	0.02
Off-physical sea s quark mass	0.84	0.69	0.79	0.20	0.39	0.91	0.28	0.19	0.42
Fit-range	0.44	2.31	0.26	0.10	1.74	0.58	3.14	0.00	1.54
Total systematic error	7.38	7.09	3.00	6.90	6.94	3.66	16.34	9.39	4.18
Total error (incl. statistical)	7.96	7.32	3.42	9.37	7.61	4.97	19.05	10.61	7.15

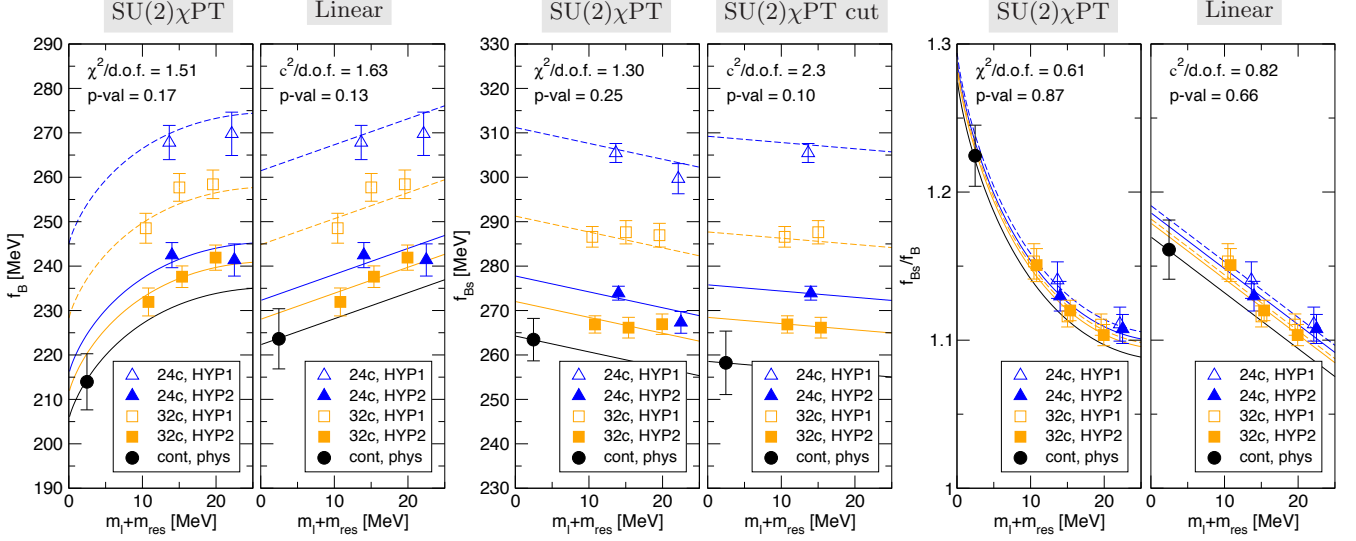


FIG. 3. Chiral fit of f_B , f_{B_s} and f_{B_s}/f_B using $SU(2)\chi PT$ and linear. "cut" indicates heaviest quark mass points at each lattice spacing are removed in the fitting.

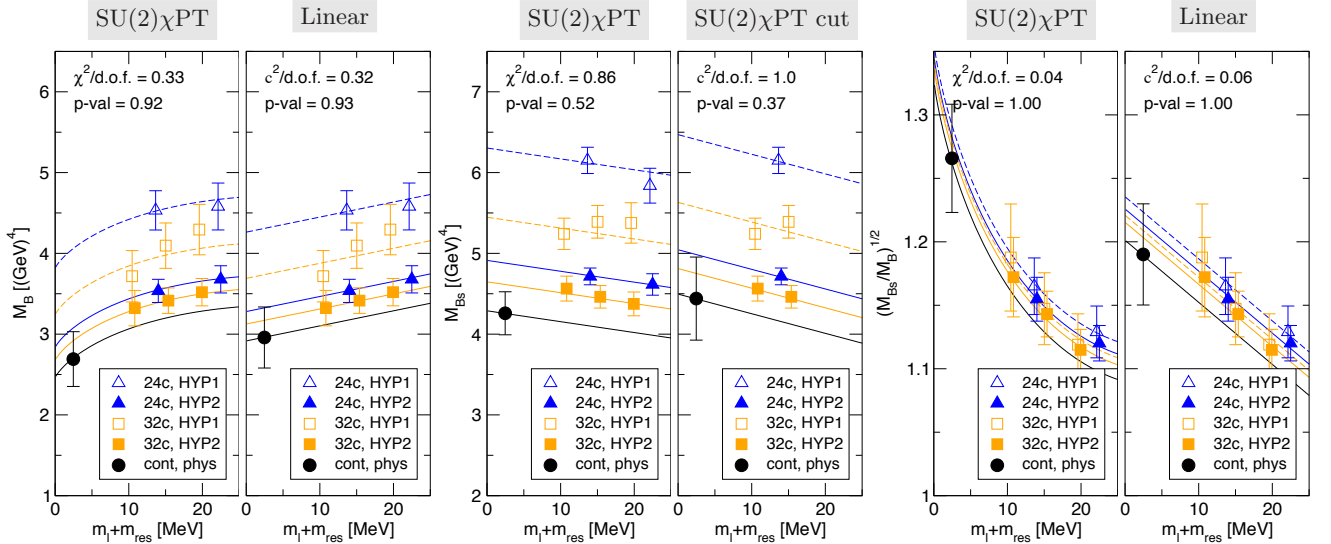


FIG. 4. Chiral fit of M_B , M_{B_s} and $(M_{B_s}/M_B)^{1/2}$ using $SU(2)\chi PT$ and linear. "cut" indicates heaviest quark mass points at each lattice spacing are removed in the fitting.

D. Renormalization

In this work, renormalization is carried out in one-loop perturbation framework. We here use power counting for the estimation of higher order uncertainty of the perturbation. We use two-step matching procedure; first, QCD full theory and HQET are matched in the continuum at a scale $\mu = m_b$, second, continuum and lattice HQET are matched at a scale $\mu = a^{-1}$. Values of α_s

in these matchings are presented in Tab. XIII. Assuming coefficients of the power expansion to be one, the counting estimation shows two-loop uncertainty of 5.1% in the first matching and of 3.1% in the second. We add them in quadrature leading to 6%. For the ratio of decay constants, the renormalization factor is completely canceled out, thus the perturbation ambiguity is negligible. For ξ , however, non-vanishing contribution Z_2/Z_1 remains in the ratio, which causes an uncertainty. Never-

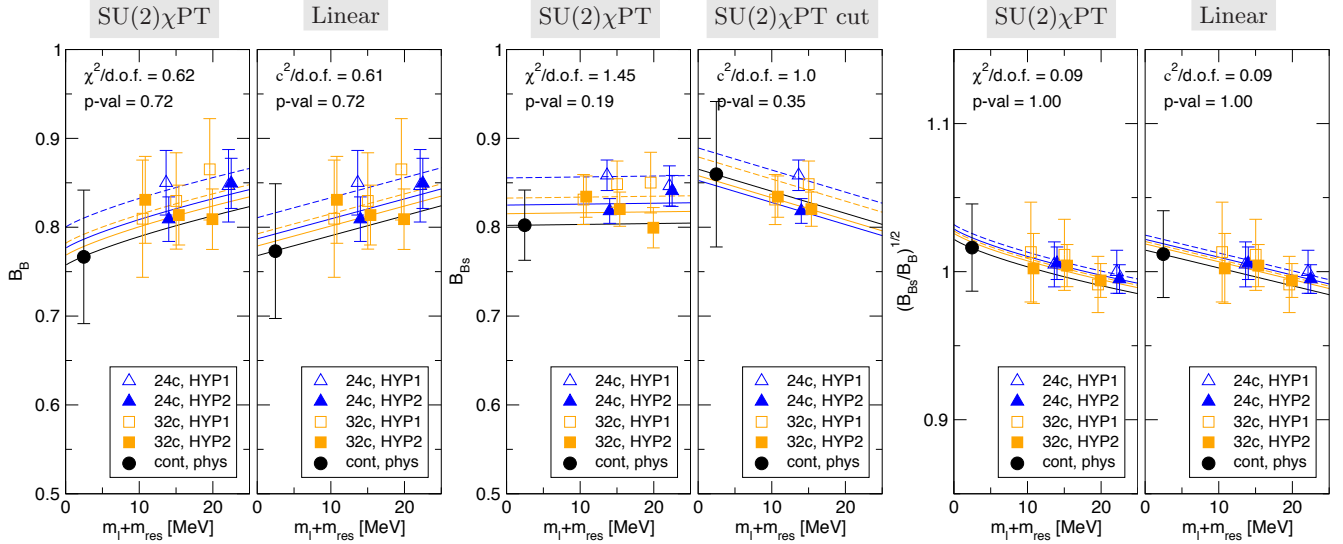


FIG. 5. Chiral fit of B_B , B_{B_s} and $(B_{B_s}/B_B)^{1/2}$ using $SU(2)\chi PT$ and linear. "cut" indicates heaviest quark mass points at each lattice spacing are removed in the fitting.

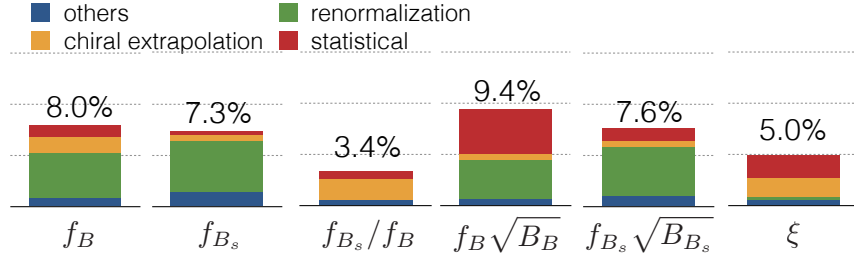


FIG. 6. Error budget for final quantities. The height of the bars denotes total error, while relative size of the colors is determined by squared errors.

TABLE XIII. Power counting for perturbation and discretization error estimation. We here define $\hat{a} = a\Lambda_{QCD}$.

$\alpha_s(m_b)$	0.2261	
$(\alpha_s(m_b))^2$	0.0511	
	24c	32c
α_s^{LAT}	0.1769	0.1683
$(\alpha_s^{LAT})^2$	0.0313	0.0283
\hat{a}	0.29	0.22
\hat{a}^2	0.084	0.048
\hat{a}^3	0.024	0.011
$\alpha_s^{LAT} \hat{a}$	0.051	0.037
$(\alpha_s^{LAT})^2 \hat{a}$	0.0091	0.0062
$\alpha_s^{LAT} \hat{a}^3$	0.0042	0.0019
$\hat{a}^2 : \alpha_s^{LAT} \hat{a} : \alpha_s^{LAT} \hat{a}^3$	1 : 0.61 : 0.05	1 : 0.77 : 0.04
$\hat{a}^2 : (\alpha_s^{LAT})^2 \hat{a} : \alpha_s^{LAT} \hat{a}^3$	1 : 0.11 : 0.05	1 : 0.13 : 0.04

theless, because this uncertainty is suppressed by a factor of $(m_s - m_l)/\Lambda_{QCD} \sim 0.2$, the one-loop ambiguity is re-

duced to 1.2%. We note that one-loop perturbation ambiguity exists also in the $O(a)$ improvement coefficients, which is counted as the discretization error as discussed the previous subsection.

E. Scale

As shown in Tab. I, lattice scales used in this study have 1% level uncertainty. We investigate systematic error from this by varying the value of lattice spacing within the uncertainty. While matching factors and $O(a)$ improved coefficients need to be implicitly varied for this search, the effect is negligible. Thus we take into account the error only when the lattice units are converted into physical units and chiral/continuum extrapolations are carried out.

F. Light quark mass

Light quark masses at physical point also have 3% level uncertainty as seen in Tab. IV. It affects values of physical observables. We check the effects by varying the physical quark mass values within the uncertainty.

G. Off physical sea s quark mass

Our gluon ensemble has only one dynamical s quark mass parameter, which is slightly off from the physical s quark mass. In spite of this, we use $SU(2)\chi PT$ fit functions assuming the sea s quark is on physical mass. The uncertainty from this inconsistency must be investigated. To deal with it, we make an estimation using $SU(3)\chi PT$ as a model. We use partially quenched $SU(3)HM\chi PT$ [47, 48], whose explicit formula are also presented in Ref. [40]. The ambiguity from off-physical s quark mass effect is investigated by taking the difference between correct treatment of our simulation setup and fake treatment where the s quark mass is assumed to be on physical point.

H. Finite volume

FV effect is estimated using $FV\chi PT$ as mentioned in Sec. VII. Uncertainty from FV effect is estimated from the difference between $SU(2)\chi PT$ and FV $SU(2)\chi PT$. The effect for B_s quantities is expected to be significantly small, thus is neglected in our analysis.

I. Fit-range dependence

As mentioned in Sec. VIE, our correlator fit results have non-negligible fit-range dependence. Although this uncertainty is rather statistical than systematic, we count it as a systematic error here. To take into account the uncertainty of the fit range choices, we shift the minimal value of t in the fit range toward larger value by 2 for two-point functions and shorten the range by 2 for three-point functions. In Appendix B, the physical quantities with the original and the shifted fit range at each simulation parameters are shown in Figs. 16, 17 and 18. We find non-negligible fit range dependences remain in some cases, where the cases that the difference between fit range choices is beyond $1\text{-}\sigma$ statistical error are listed in the caption in each figure. We define the uncertainty of the fit range dependences as:

1. When physical quantities at some quark mass parameter move beyond 1σ statistical error by changing the fit range, the data at the mass parameter for both HYP1 and HYP2 are replaced to see the effect of the move.

2. Chiral/continuum fits are performed to investigate the shift caused by the replacement of the data.
3. We repeat this procedure for each data which has large move beyond $1\text{-}\sigma$ statistical error by changing the fit range.
4. The final uncertainty is obtained by adding each shift of the chiral/continuum extrapolated value in quadrature.

The resulting uncertainty is taken as a systematic error in our calculation.

IX. CONCLUSIONS

A. Results of physical quantities

We present final results for B meson quantities in the static limit of b quark:

$$[f_B]^{\text{static}} = 218.8(6.5)_{\text{stat}}(16.1)_{\text{sys}} \text{ MeV}, \quad (137)$$

$$[f_{B_s}]^{\text{static}} = 263.5(4.8)_{\text{stat}}(18.7)_{\text{sys}} \text{ MeV}, \quad (138)$$

$$[f_{B_s}/f_B]^{\text{static}} = 1.193(20)_{\text{stat}}(36)_{\text{sys}}, \quad (139)$$

$$\left[f_B\sqrt{\hat{B}_B}\right]^{\text{static}} = 240(15)_{\text{stat}}(17)_{\text{sys}} \text{ MeV}, \quad (140)$$

$$\left[f_{B_s}\sqrt{\hat{B}_{B_s}}\right]^{\text{static}} = 290(09)_{\text{stat}}(20)_{\text{sys}} \text{ MeV}, \quad (141)$$

$$[\xi]^{\text{static}} = 1.208(41)_{\text{stat}}(44)_{\text{sys}}, \quad (142)$$

$$[\hat{B}_B]^{\text{static}} = 1.17(11)_{\text{stat}}(19)_{\text{sys}}, \quad (143)$$

$$[\hat{B}_{B_s}]^{\text{static}} = 1.22(06)_{\text{stat}}(11)_{\text{sys}}, \quad (144)$$

$$[B_{B_s}/B_B]^{\text{static}} = 1.028(60)_{\text{stat}}(43)_{\text{sys}}, \quad (145)$$

where first errors indicate statistical while second ones are systematic. Note that $O(1/m_b)$ uncertainty, which is mentioned in the next subsection, is not included in the systematic errors above. We also show final results including $O(1/m_b)$ uncertainty in the systematic error:

$$f_B = 218.8(6.5)_{\text{stat}}(30.8)_{\text{sys}} \text{ MeV}, \quad (146)$$

$$f_{B_s} = 263.5(4.8)_{\text{stat}}(36.7)_{\text{sys}} \text{ MeV}, \quad (147)$$

$$f_{B_s}/f_B = 1.193(20)_{\text{stat}}(44)_{\text{sys}}, \quad (148)$$

$$f_B\sqrt{\hat{B}_B} = 240(15)_{\text{stat}}(33)_{\text{sys}} \text{ MeV}, \quad (149)$$

$$f_{B_s}\sqrt{\hat{B}_{B_s}} = 290(09)_{\text{stat}}(40)_{\text{sys}} \text{ MeV}, \quad (150)$$

$$\xi = 1.208(41)_{\text{stat}}(52)_{\text{sys}}, \quad (151)$$

$$\hat{B}_B = 1.17(11)_{\text{stat}}(24)_{\text{sys}}, \quad (152)$$

$$\hat{B}_{B_s} = 1.22(06)_{\text{stat}}(19)_{\text{sys}}, \quad (153)$$

$$B_{B_s}/B_B = 1.028(60)_{\text{stat}}(49)_{\text{sys}}. \quad (154)$$

We here present the constraint on a ratio of CKM matrix element (2) obtained through Eq. (12):

$$\left| \frac{V_{td}}{V_{ts}} \right| = 0.206(13), \quad (155)$$

where statistical and systematic errors including $O(1/m_b)$ uncertainty are all added in quadrature.

B. Comparison with other approaches and $1/m_b$ ambiguity

Since we use static approximation for b quark, there exists $O(\Lambda_{\text{QCD}}/m_b)$ uncertainty for the physical quantities. Here, we take PDG value of b quark mass in $\overline{\text{MS}}$ scheme $m_b = 4.18(03)$ GeV [15] and assume $\Lambda_{\text{QCD}} = 0.5$ GeV. The uncertainty from static approximation becomes 12%. For the SU(3) breaking ratios, however, there would be suppression factor coming from SU(3) light flavor symmetry, which leads:

$$\frac{\Lambda_{\text{QCD}}}{m_b} \times \frac{m_s - m_d}{\Lambda_{\text{QCD}}} \sim 2.2\%. \quad (156)$$

We show comparison with other works for our obtained quantities in Figs. 7, 8 and 9. (See also Review of lattice results by Flavor Lattice Averaging Group (FLAG) [49].) Our results have $\sim 10\%$ larger value for decay constants f_B and f_{B_s} from other works at physical b quark mass point, which would be plausibly understood by the static approximation ambiguity. The ETM Collaboration's results at the static limit in Ref. [50] also shows this tendency. However, ALPHA Collaboration's results on f_B and f_{B_s} in the static limit indicate much smaller deviation from those at physical b quark mass point [12]. We cannot conclude the reason of this difference from us, because our current uncertainty is still large. On the other hand, there is no clear difference from the physical b quark point in $f_B\sqrt{\hat{B}_B}$, $f_{B_s}\sqrt{\hat{B}_{B_s}}$, \hat{B}_B and \hat{B}_{B_s} , because of the large error. For the SU(3) breaking ratios, significant deviation from others is not seen, since the static approximation uncertainty is largely reduced by SU(3) light flavor symmetry factor as described in Eq. (156).

Finally, it would be interesting to see a correspondence between ξ and f_{B_s}/f_B . In this study we obtained the difference:

$$\Delta = \xi - \frac{f_{B_s}}{f_B} = 0.015(73), \quad (157)$$

where correlation between ξ and f_{B_s}/f_B is omitted. As mentioned in Sec. III A, naive factorization suggests ξ is close to f_{B_s}/f_B , and our result supports this observation in the static limit of b quark. In Fig. 10 we show Δ in other works together with our results. No discrepancy between ξ and f_{B_s}/f_B beyond 1σ error has yet been seen.

C. Further improvements for next step

Although the obtained results in this work is encouraging, there exist limitations due to insufficient statistics and various systematic errors. As the current error budget in Fig. 6 shows, dominant uncertainties are statistical error, chiral extrapolation and uncertainty from renormalization. To overcome the current situation, possible options are following.

All-Mode-Averaging (AMA): Currently, our results have large statistical error and chiral extrapolation is suffering from the lack of statistics. Gluon link smearings in the static action help to improve signal qualities to some extent, the statistical error is, however, not enough small. All-mode-averaging (AMA) technique [60] provides a substantial computational cost reduction, which leads to the improved statistics. In the AMA, a bunch of source points are put to increase statistics keeping computational cost small by using a conjugate gradient (CG) solver with relaxed convergence conditions.

Physical light quark mass point simulation:

The lightest pion mass in this paper is ~ 290 [MeV], which leaves large uncertainty from the chiral extrapolation. This error would be significantly reduced by the physical point simulation, where the simulated pion mass is ~ 135 [MeV]. The 2+1 flavor dynamical ensembles are being generated by RBC/UKQCD Collaborations using Möbius DWF [61], keeping almost the same lattice spacings as those in this work, but with doubled physical volume [62]. It would increase computational cost by a large amount, hence the AMA technique mentioned above is crucial.

Non-perturbative renormalization: While one-loop renormalization uncertainty is 0% or quite small for SU(3) breaking ratios, it is estimated to be, at the most, 6% for non-ratio quantities. Non-perturbative renormalization is, hence, required for the non-ratio quantities to reduce the large uncertainty. The renormalization would be accomplished using the momentum-subtraction (RI/MOM) scheme [63, 64], in which an additional renormalization condition is required to manage the $1/a$ power divergence.

These programs are non-trivial but promising directions. Part of them are currently on-going [65] and we plan to present more definite results on this project in near future.

ACKNOWLEDGMENTS

We thank members of RBC/UKQCD Collaborations, especially Oliver Witzel for useful discussions. The calculations reported here were performed on the QCDOC computers of RIKEN-BNL Research Center and

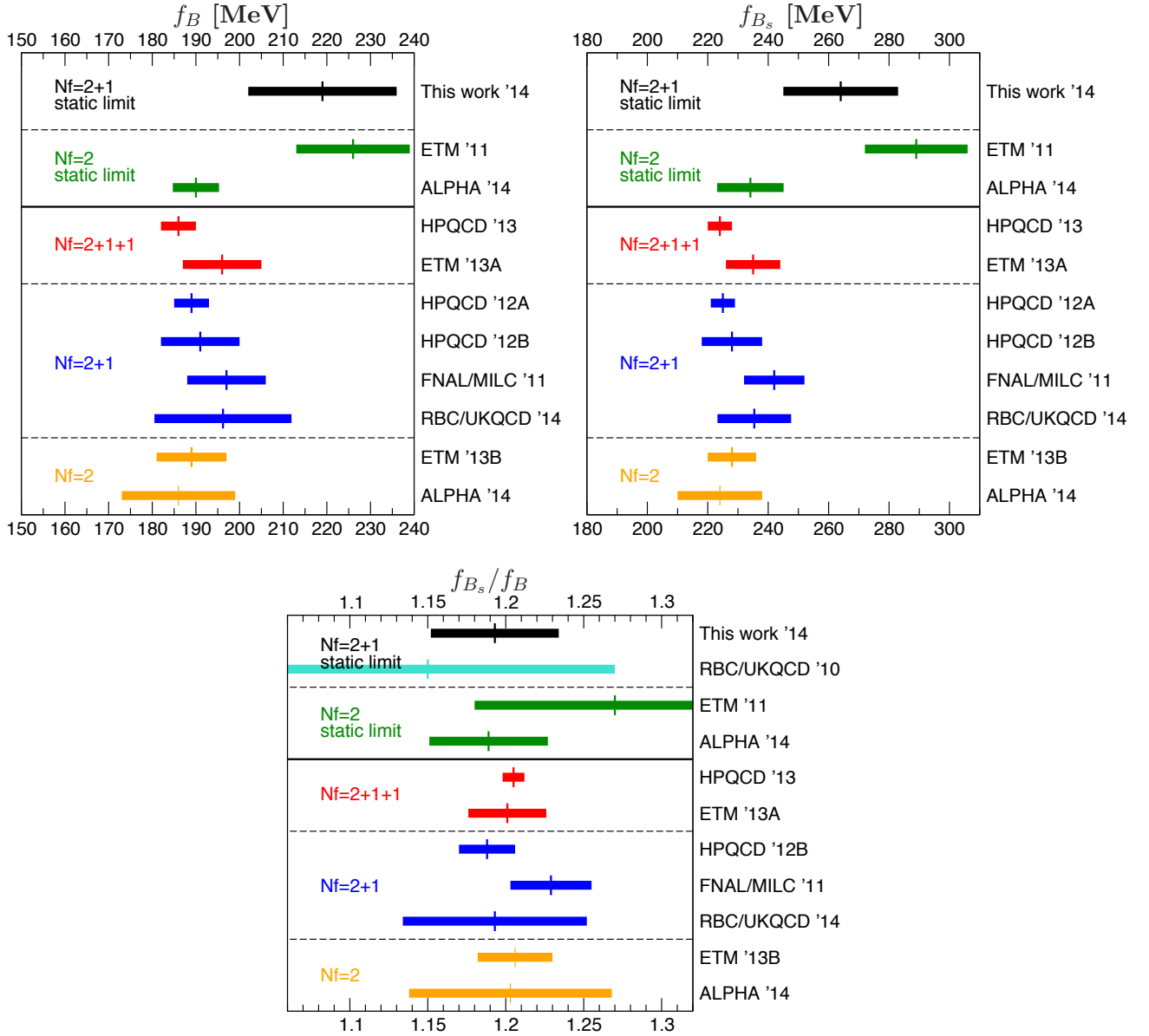


FIG. 7. Comparison of f_B , f_{B_s} and f_{B_s}/f_B with other works. The data is cited from Refs. [50] (ETM '11), [12] (ALPHA '14), [51] (HPQCD '13), [52] (ETM '13A), [53, 54] (HPQCD '12A, HPQCD '12B), [55] (FNAL/MILC '11), [56] (RBC/UKQCD '14), [14] (ETM '13B) and [40] (RBC/UKQCD '10). The values of f_B and f_{B_s} in ETM '11 are obtained from Φ_B and Φ_{B_s} divided by $\sqrt{m_B}$ and $\sqrt{m_{B_s}}$, respectively. Errors for the static limit results do not contain $1/m_b$ uncertainty.

the USQCD Collaboration at Brookhaven National Laboratory (BNL), RIKEN Integrated Cluster of Clusters (RICC) at RIKEN, Wako, KMI computer φ at Nagoya University and resources provided by the USQCD Collaboration funded by the U.S. Department of Energy. The software used includes the CPS QCD codes (<http://qcdoc.phys.columbia.edu/cps.html>), supported in part by the U.S. DOE SciDAC program. This work is supported in part by JSPS Kakenhi grant Nos. 21540289 and 22224003 (Y. A.). T. Izubuchi, C. L. and A. S. were supported in part by U.S. DOE con-

tract DE-AC02-98CH10886 and T. Izubuchi also by JSPS Grants 22540301, 23105715 and 26400261.

Appendix A: Effective mass and correlator plots

Figs. 11–15 show effective mass plots in two-point function and three-point function plots. The fit ranges and fit results are included in the figures.

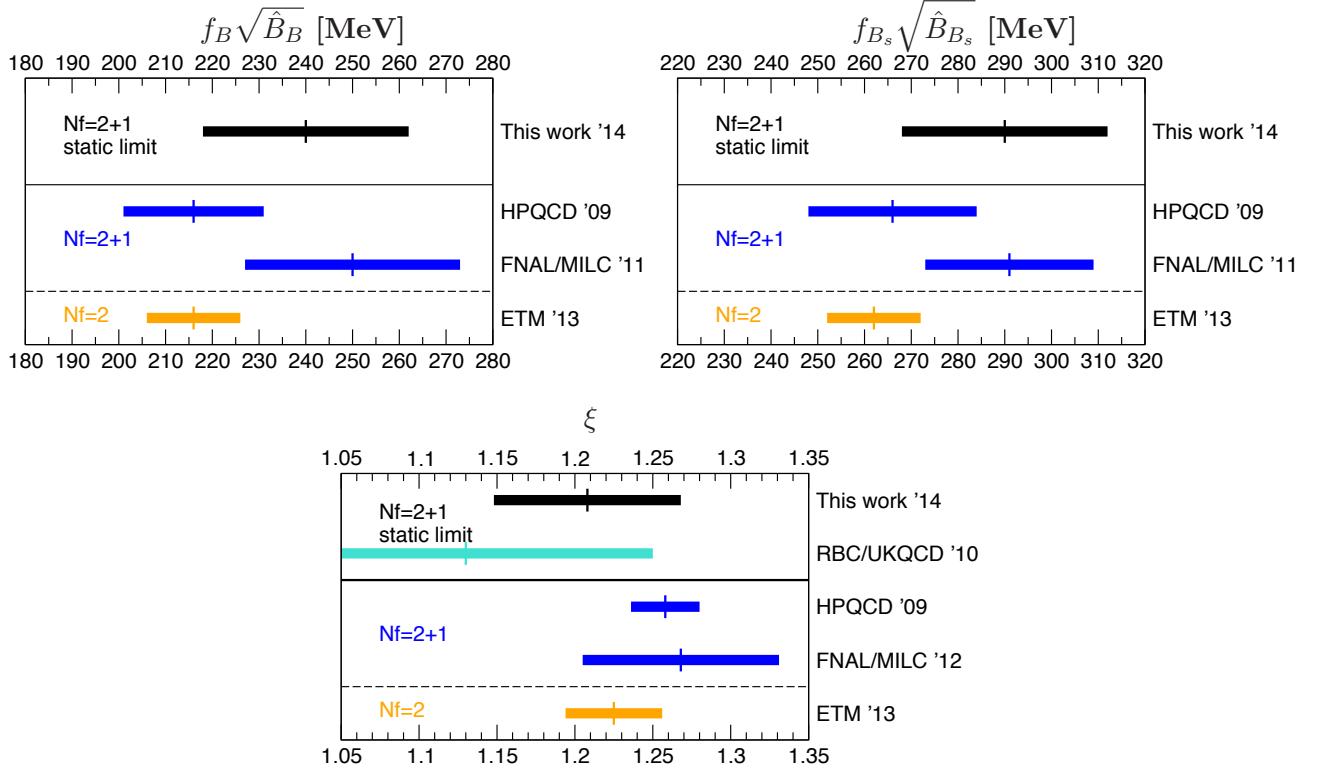


FIG. 8. Comparison of $f_B \sqrt{\hat{B}_B}$, $f_{B_s} \sqrt{\hat{B}_{B_s}}$ and ξ with other works. The data is cited from Refs. [57] (HPQCD '09), [58] (FNAL/MILC '11), [59] (FNAL/MILC '12), [14] (ETM '13) and [40] (RBC/UKQCD '10). The RGI value of $f_B \sqrt{\hat{B}_B}$ and $f_{B_s} \sqrt{\hat{B}_{B_s}}$ in FNAL/MILC '11 are obtained by converting $f_B \sqrt{B_B}$ and $f_{B_s} \sqrt{B_{B_s}}$ at $\mu = m_b$ in Ref. [58] with the two-loop multiplicative factor 1.516. Errors for the static limit results do not contain $1/m_b$ uncertainty.

Appendix B: Fit range dependence

We show fit range dependences of physical quantities at each simulation point in Figs. 16, 17 and 18. To check the dependences, we shift the minimal value of t in the fit range toward larger value by 2 for two-point functions and shorten the range by 2 for three-point functions, which we name “fit range 2” in the figures. To be more specific, the actual fit ranges are:

$$\begin{aligned}
 &\text{original (24c)} : t = 10 - 15 (\bar{\text{LS}}, \bar{\text{SS}}), t = 13 - 18 (\text{SS}), \\
 &\quad t = 7 - 13 (\text{VV} + \text{AA}, \text{SS} + \text{PP}), \\
 &\text{original (32c)} : t = 10 - 16 (\bar{\text{LS}}, \bar{\text{SS}}), t = 13 - 19 (\text{SS}), \\
 &\quad t = 9 - 15 (\text{VV} + \text{AA}, \text{SS} + \text{PP}), \\
 &\text{fit range 2 (24c)} : t = 12 - 15 (\bar{\text{LS}}, \bar{\text{SS}}), t = 15 - 18 (\text{SS}), \\
 &\quad t = 8 - 12 (\text{VV} + \text{AA}, \text{SS} + \text{PP}), \\
 &\text{fit range 2 (32c)} : t = 12 - 16 (\bar{\text{LS}}, \bar{\text{SS}}), t = 15 - 19 (\text{SS}), \\
 &\quad t = 10 - 14 (\text{VV} + \text{AA}, \text{SS} + \text{PP}).
 \end{aligned}$$

We find disagreements between choices of fit range beyond 1- σ statistical error for some cases.

[1] M. Kobayashi and T. Maskawa, Prog. Theor. Phys. **49**, 652 (1973).

[2] T. Inami and C. S. Lim, Prog. Theor. Phys. **65**, 297 (1981) [Erratum-ibid. **65**, 1772 (1981)].

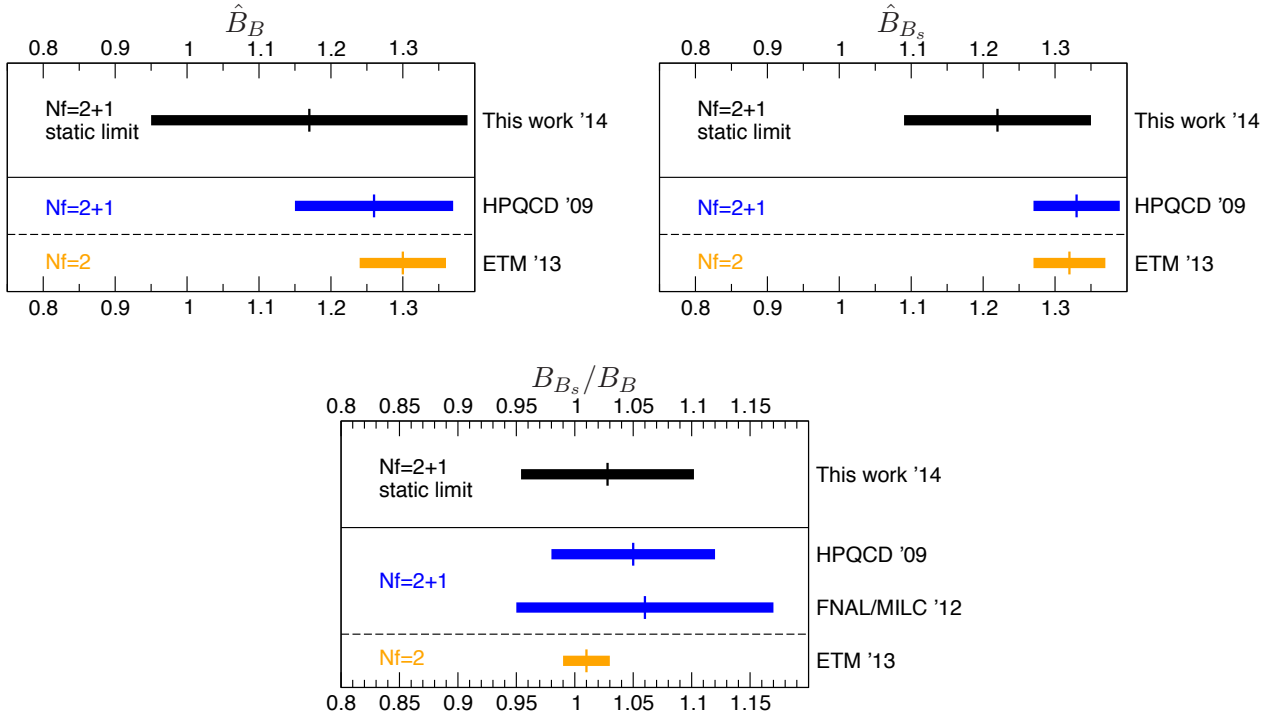


FIG. 9. Comparison of \hat{B}_B , \hat{B}_{B_s} and B_{B_s}/B_B with other works. The data is cited from Refs. [57] (HPQCD '09), [14] (ETM '13) and [59] (FNAL/MILC '12). Errors for the static limit results do not contain $1/m_b$ uncertainty.

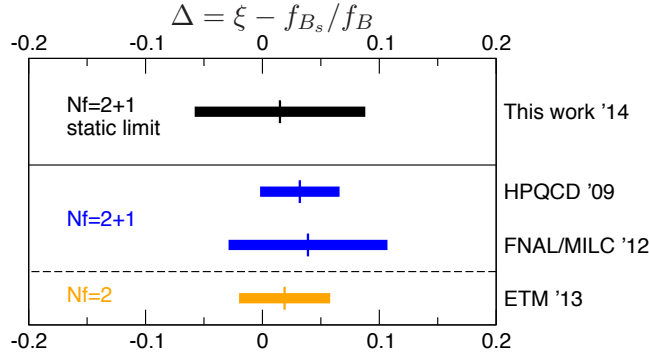


FIG. 10. Comparison of $\Delta = \xi - f_{B_s}/f_B$ with other works. The data is cited from Refs. [57] (HPQCD '09), [59] (FNAL/MILC '12) and [14] (ETM '13). In calculating Δ , correlations between ξ and f_{B_s}/f_B are not taken into account.

- [3] C. W. Bernard, T. Blum and A. Soni, Phys. Rev. D **58**, 014501 (1998) [hep-lat/9801039].
- [4] E. Eichten and B. R. Hill, Phys. Lett. B **234**, 511 (1990).
- [5] E. Eichten and B. R. Hill, Phys. Lett. B **240**, 193 (1990).
- [6] G. P. Lepage, Nucl. Phys. Proc. Suppl. **26**, 45 (1992).
- [7] M. Della Morte *et al.* [ALPHA Collaboration], Phys. Lett. B **581**, 93 (2004) [Erratum-ibid. B **612**, 313 (2005)] [hep-lat/0307021].
- [8] M. Della Morte, A. Shindler and R. Sommer, JHEP **0508**, 051 (2005) [arXiv:hep-lat/0506008].
- [9] L. Maiani, G. Martinelli and C. T. Sachrajda, Nucl. Phys. B **368**, 281 (1992).
- [10] J. Heitger *et al.* [ALPHA Collaboration], JHEP **0402**, 022 (2004) [hep-lat/0310035].
- [11] C. W. Bernard, J. N. Labrenz and A. Soni, Phys. Rev. D **49**, 2536 (1994) [hep-lat/9306009].
- [12] F. Bernardoni, B. Blossier, J. Bulava, M. Della Morte, P. Fritzsch, N. Garron, A. Gérardin and J. Heitger *et al.*, arXiv:1404.3590 [hep-lat].
- [13] B. Blossier *et al.* [ETM Collaboration], JHEP **1004**, 049 (2010) [arXiv:0909.3187 [hep-lat]].
- [14] N. Carrasco *et al.* [ETM Collaboration], JHEP **1403**, 016 (2014) [arXiv:1308.1851 [hep-lat]].

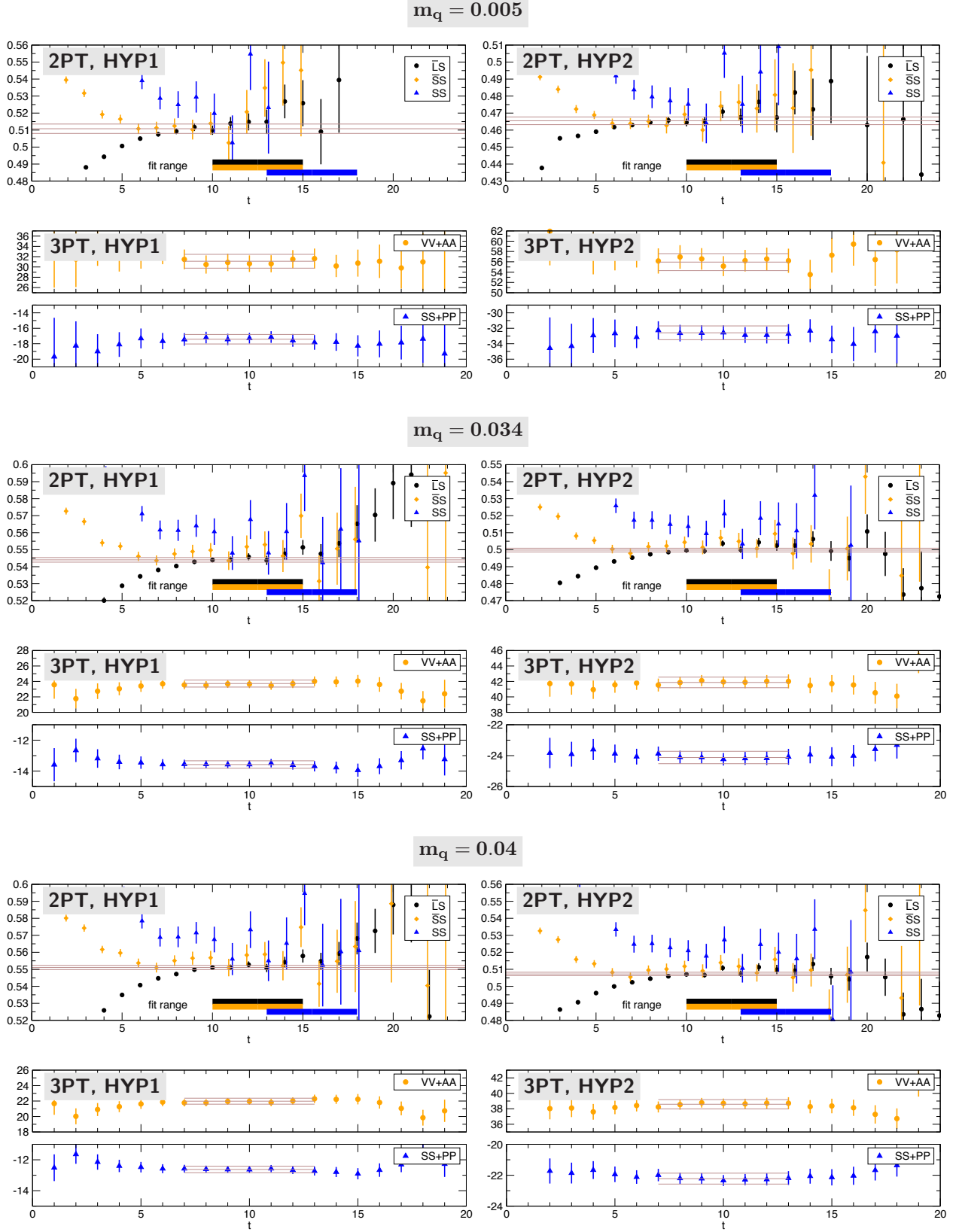


FIG. 11. Effective mass (two-point function) and three-point function plot for 24c1. The figures show $E_{\text{eff}} = -\ln(C^{\text{XX}}(t+1,0)/C^{\text{XX}}(t,0))$ with $\text{XX} = (\bar{L}S, \bar{S}S, SS)$ for 2PT, $C_L^{SS}(t_f, t, 0)$ for 3PT VV+AA and $C_S^{SS}(t_f, t, 0)$ for 3PT SS+PP. Fit ranges and fit results are shown in the figures. For three-point functions t_f is fixed to be 20.

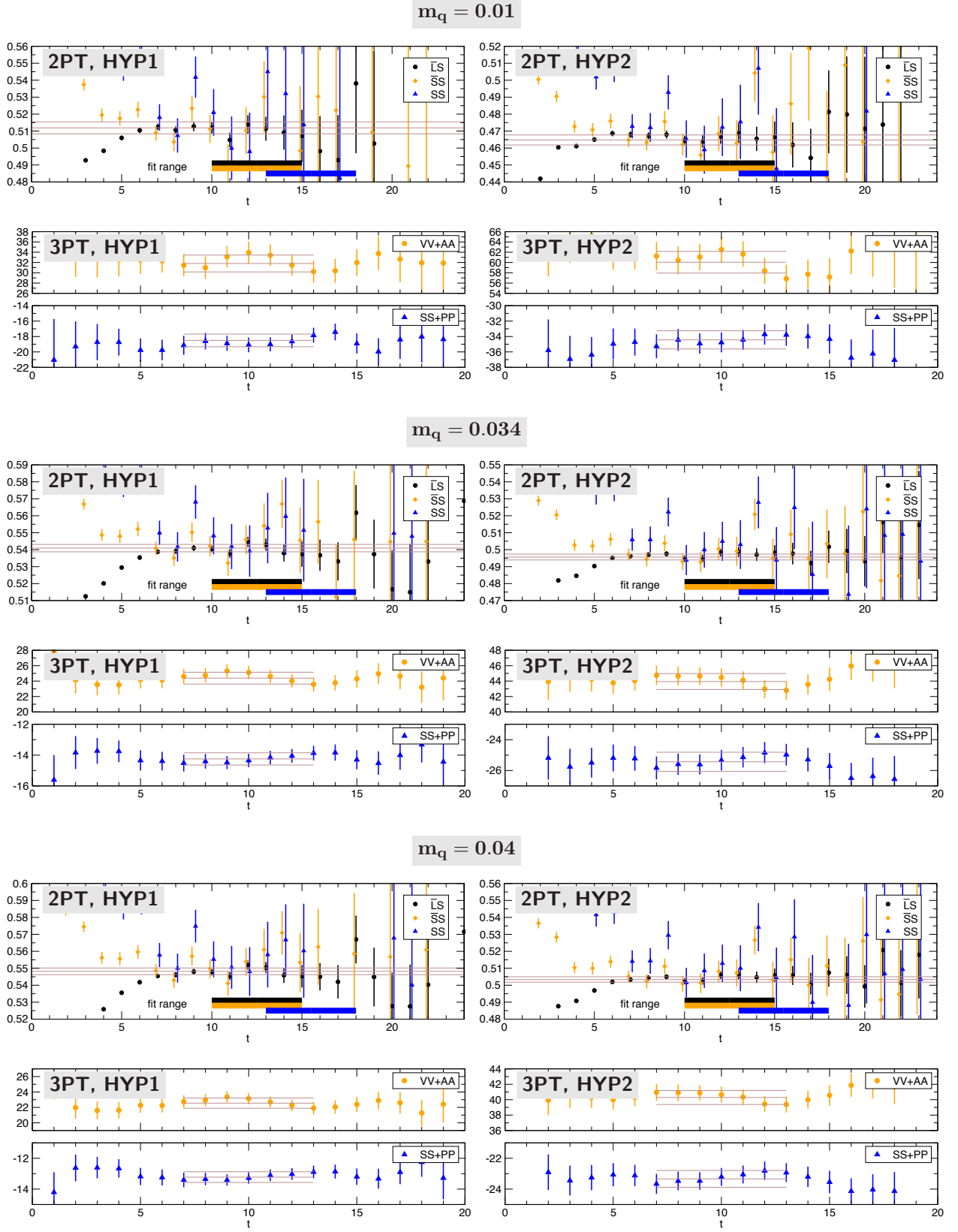


FIG. 12. Effective mass (two-point function) and three-point function plot for 24c2. The figures show $E_{\text{eff}} = -\ln(C^{\text{XX}}(t+1,0)/C^{\text{XX}}(t,0))$ with $\text{XX} = (\bar{L}S, \bar{S}S, SS)$ for 2PT, $C_L^{SS}(t_f, t, 0)$ for 3PT $VV+AA$ and $C_S^{SS}(t_f, t, 0)$ for 3PT $SS+PP$. Fit ranges and fit results are shown in the figures. For three-point functions t_f is fixed to be 20.

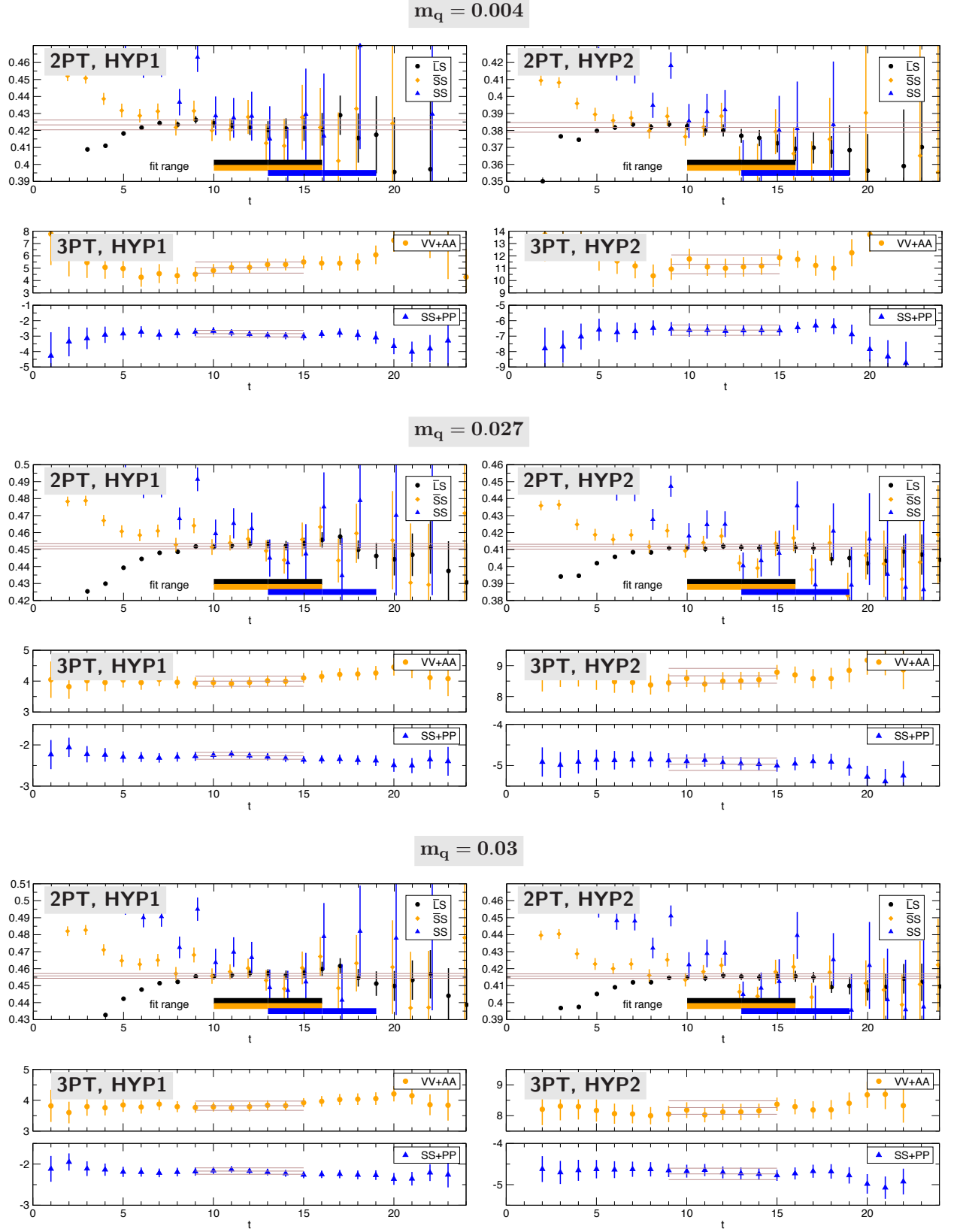


FIG. 13. Effective mass (two-point function) and three-point function plot for 32c1. The figures show $E_{\text{eff}} = -\ln(C^{\text{XX}}(t+1,0)/C^{\text{XX}}(t,0))$ with $\text{XX} = (\bar{L}S, \bar{S}S, SS)$ for 2PT, $C_L^{SS}(t_f, t, 0)$ for 3PT VV+AA and $C_S^{SS}(t_f, t, 0)$ for 3PT SS+PP. Fit ranges and fit results are shown in the figures. For three-point functions t_f is fixed to be 24.

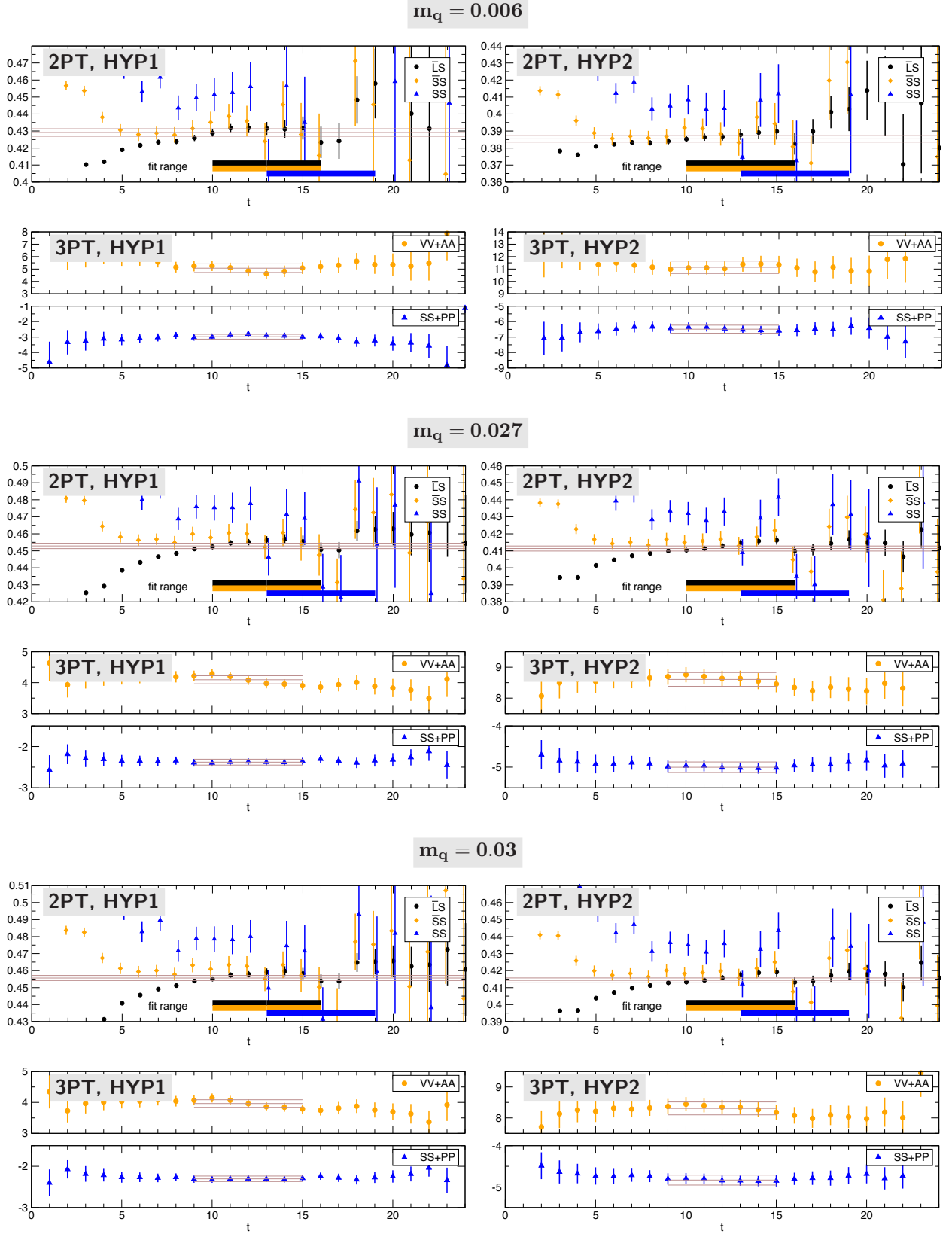


FIG. 14. Effective mass (two-point function) and three-point function plot for 32c2. The figures show $E_{\text{eff}} = -\ln(C^{\text{XX}}(t+1,0)/C^{\text{XX}}(t,0))$ with $\text{XX} = (\bar{L}S, \bar{S}S, SS)$ for 2PT, $C_L^{SS}(t_f, t, 0)$ for 3PT VV+AA and $C_S^{SS}(t_f, t, 0)$ for 3PT SS+PP. Fit ranges and fit results are shown in the figures. For three-point functions t_f is fixed to be 24.

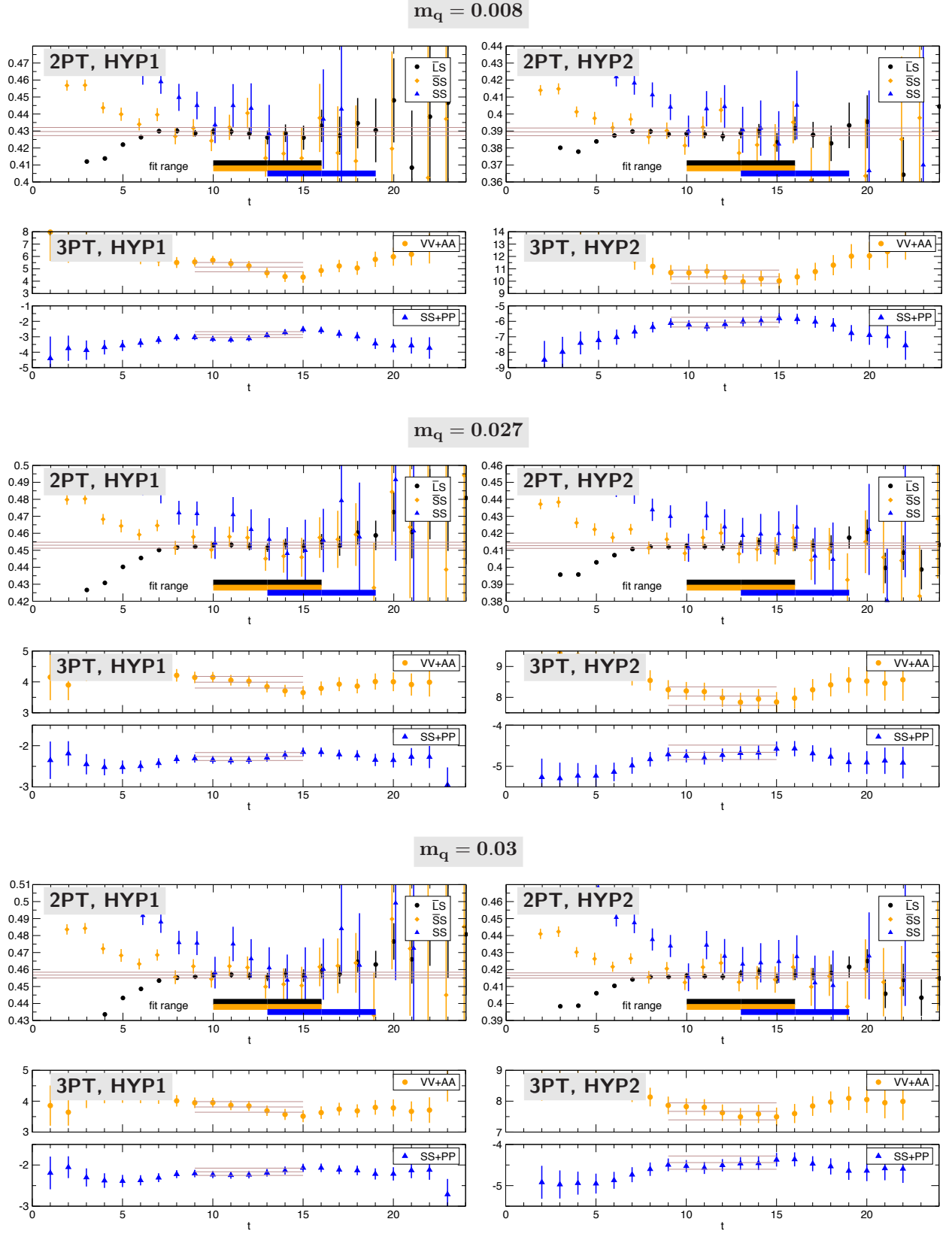


FIG. 15. Effective mass (two-point function) and three-point function plot for 32c3. The figures show $E_{\text{eff}} = -\ln(C^{\text{XX}}(t+1,0)/C^{\text{XX}}(t,0))$ with $\text{XX} = (\bar{L}S, \bar{S}S, SS)$ for 2PT, $C_L^{SS}(t_f, t, 0)$ for 3PT VV+AA and $C_S^{SS}(t_f, t, 0)$ for 3PT SS+PP. Fit ranges and fit results are shown in the figures. For three-point functions t_f is fixed to be 24.

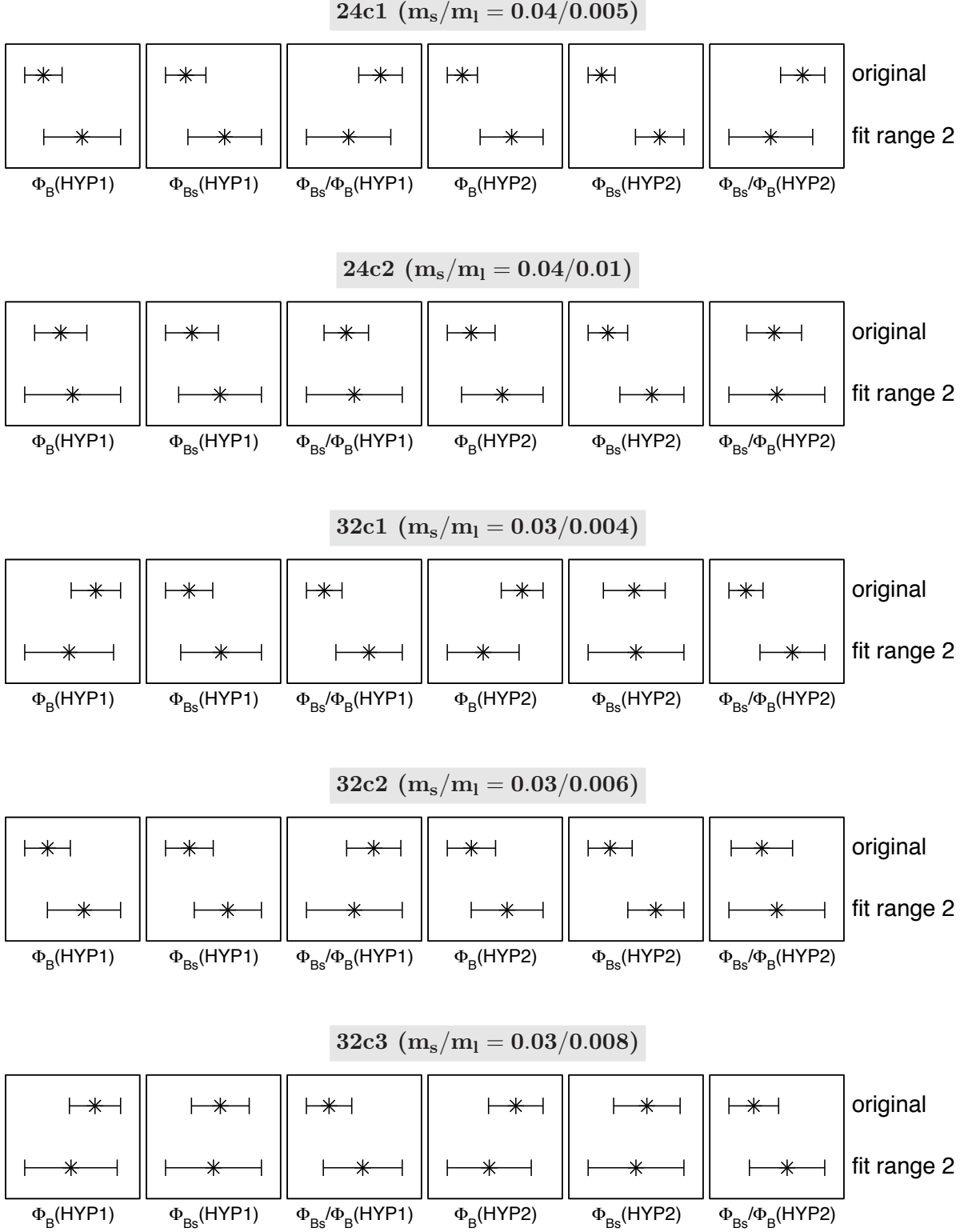


FIG. 16. Fit range dependence of Φ_B , Φ_{Bs} and Φ_{Bs}/Φ_B at each simulation point. Horizontal labels are suppressed. We find differences between fit range choices beyond $1\text{-}\sigma$ statistical error in $24c1(\Phi_B, \Phi_{Bs})$, $24c2(\Phi_{Bs})$, $32c1(\Phi_B, \Phi_{Bs}/\Phi_B)$ and $32c2(\Phi_{Bs})$.

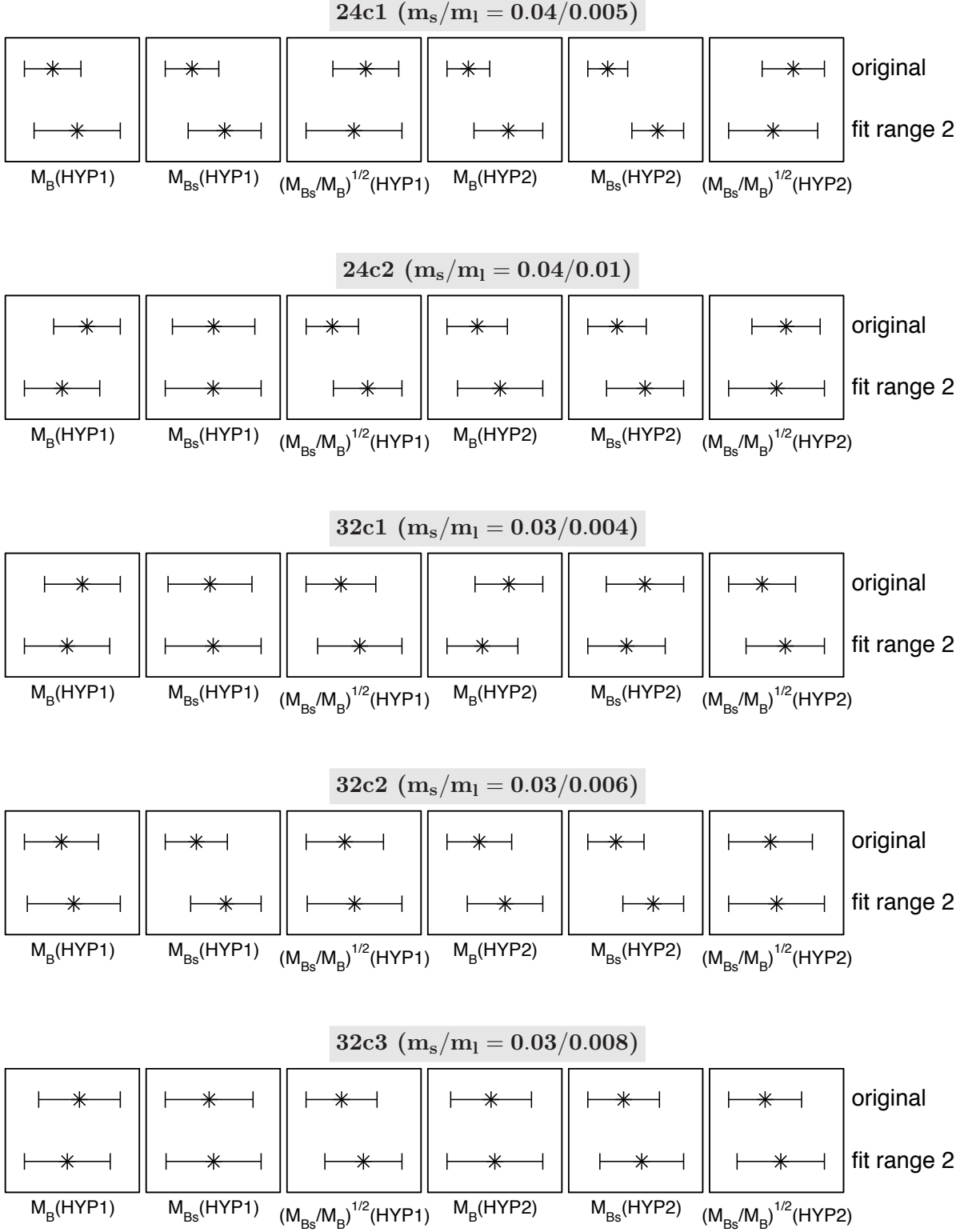


FIG. 17. Fit range dependence of M_B , M_{B_s} and $(M_{B_s}/M_B)^{1/2}$ at each simulation point. Horizontal labels are suppressed. We find differences between fit range choices beyond $1\text{-}\sigma$ statistical error in 24c1(M_B, M_{B_s}), 24c2($(M_{B_s}/M_B)^{1/2}$) and 32c2(M_{B_s}).

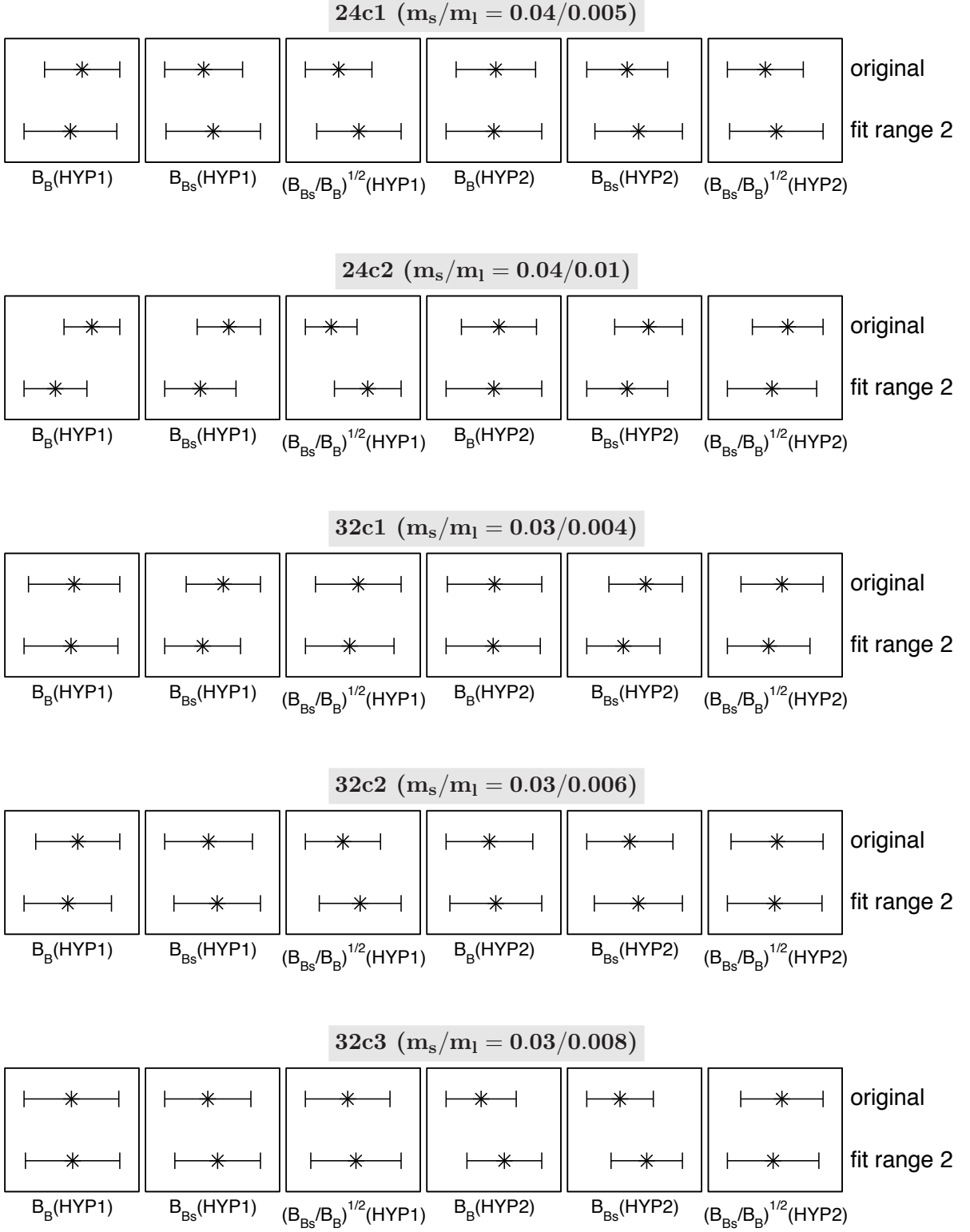


FIG. 18. Fit range dependence of B_B , B_{B_s} and $(B_{B_s}/B_B)^{1/2}$ at each simulation point. Horizontal labels are suppressed. We find differences between fit range choices beyond $1\text{-}\sigma$ statistical error in $24c2(B_B, (B_{B_s}/B_B)^{1/2})$.

- [15] J. Beringer *et al.* [Particle Data Group Collaboration], Phys. Rev. D **86**, 010001 (2012).
- [16] A. J. Buras, M. Jamin and P. H. Weisz, Nucl. Phys. B **347**, 491 (1990).
- [17] K. G. Chetyrkin, Phys. Lett. B **404**, 161 (1997) [hep-ph/9703278].
- [18] J. A. M. Vermaseren, S. A. Larin and T. van Ritbergen, Phys. Lett. B **405**, 327 (1997) [hep-ph/9703284].
- [19] A. Hasenfratz and F. Knechtli, Phys. Rev. D **64**, 034504 (2001) [arXiv:hep-lat/0103029].
- [20] D. B. Kaplan, Phys. Lett. B **288**, 342 (1992) [arXiv:hep-lat/9206013].
- [21] R. Narayanan and H. Neuberger, Phys. Lett. B **302**, 62 (1993) [arXiv:hep-lat/9212019].
- [22] Y. Shamir, Nucl. Phys. B **406**, 90 (1993) [arXiv:hep-lat/9303005].
- [23] J. Noaki and Y. Taniguchi, Phys. Rev. D **61**, 054505 (2000) [arXiv:hep-lat/9906030].
- [24] Y. Iwasaki, Nucl. Phys. B **258**, 141 (1985).
- [25] Y. Iwasaki, UTHEP-118.
- [26] Y. Aoki *et al.* [RBC and UKQCD Collaborations], Phys. Rev. D **83**, 074508 (2011) [arXiv:1011.0892 [hep-lat]].
- [27] A. J. Buras and P. H. Weisz, Nucl. Phys. B **333** (1990) 66.
- [28] J. M. Flynn, O. F. Hernandez and B. R. Hill, Phys. Rev. D **43**, 3709 (1991).
- [29] G. Buchalla, Phys. Lett. B **395**, 364 (1997) [arXiv:hep-ph/9608232].
- [30] T. Ishikawa, Y. Aoki, J. M. Flynn, T. Izubuchi, O. Laktik and , JHEP **1105**, 040 (2011) [arXiv:1101.1072 [hep-lat]].
- [31] X. D. Ji and M. J. Musolf, Phys. Lett. B **257**, 409 (1991).
- [32] D. J. Broadhurst and A. G. Grozin, Phys. Lett. B **267**, 105 (1991) [arXiv:hep-ph/9908362].
- [33] V. Gimenez, Nucl. Phys. B **401**, 116 (1993).
- [34] M. Ciuchini, E. Franco and V. Gimenez, Phys. Lett. B **388**, 167 (1996) [arXiv:hep-ph/9608204].
- [35] D. Becirevic and J. Reyes, Nucl. Phys. Proc. Suppl. **129**, 435 (2004) [arXiv:hep-lat/0309131].
- [36] B. Blossier, Phys. Rev. D **76**, 114513 (2007) [arXiv:0705.0283 [hep-lat]].
- [37] M. Papinutto, G. Herdoiza, C. Pena and A. Vladikas, PoS LATTICE **2013**, 317 (2013) [arXiv:1311.5177 [hep-lat]].
- [38] G. P. Lepage and P. B. Mackenzie, Phys. Rev. D **48**, 2250 (1993) [arXiv:hep-lat/9209022].
- [39] N. H. Christ, T. T. Dumitrescu, O. Laktik and T. Izubuchi, PoS **LAT2007**, 351 (2007) [arXiv:0710.5283 [hep-lat]].
- [40] C. Albertus, Y. Aoki, P. A. Boyle, N. H. Christ, T. T. Dumitrescu, J. M. Flynn, T. Ishikawa and T. Izubuchi *et al.*, Phys. Rev. D **82**, 014505 (2010) [arXiv:1001.2023 [hep-lat]].
- [41] C. Alexandrou, S. Gusken, F. Jegerlehner, K. Schilling and R. Sommer, Nucl. Phys. B **414**, 815 (1994) [hep-lat/9211042].
- [42] F. Berruto, T. Blum, K. Orginos and A. Soni, Phys. Rev. D **73**, 054509 (2006) [hep-lat/0512004].
- [43] C. Allton *et al.* [RBC-UKQCD Collaboration], Phys. Rev. D **78**, 114509 (2008) [arXiv:0804.0473 [hep-lat]].
- [44] W. Detmold, C. -J. D. Lin and S. Meinel, Phys. Rev. Lett. **108**, 172003 (2012) [arXiv:1109.2480 [hep-lat]].
- [45] C. Bernard [MILC Collaboration], Phys. Rev. D **65**, 054031 (2002) [hep-lat/0111051].
- [46] G. Colangelo, S. Durr and C. Haefeli, Nucl. Phys. B **721**, 136 (2005) [hep-lat/0503014].
- [47] D. Arndt and C. J. D. Lin, Phys. Rev. D **70**, 014503 (2004) [hep-lat/0403012].
- [48] C. Aubin and C. Bernard, Phys. Rev. D **73**, 014515 (2006) [hep-lat/0510088].
- [49] S. Aoki, Y. Aoki, C. Bernard, T. Blum, G. Colangelo, M. Della Morte, S. Durr and A. X. E. Khadra *et al.*, arXiv:1310.8555 [hep-lat].
- [50] P. Dimopoulos *et al.* [ETM Collaboration], JHEP **1201**, 046 (2012) [arXiv:1107.1441 [hep-lat]].
- [51] R. J. Dowdall *et al.* [HPQCD Collaboration], Phys. Rev. Lett. **110**, no. 22, 222003 (2013) [arXiv:1302.2644 [hep-lat]].
- [52] N. Carrasco, P. Dimopoulos, R. Frezzotti, V. Gimenez, P. Lami, V. Lubicz, E. Picca and L. Riggio *et al.*, arXiv:1311.2837 [hep-lat].
- [53] C. McNeile, C. T. H. Davies, E. Follana, K. Hornbostel and G. P. Lepage, Phys. Rev. D **85**, 031503 (2012) [arXiv:1110.4510 [hep-lat]].
- [54] H. Na, C. J. Monahan, C. T. H. Davies, R. Horgan, G. P. Lepage and J. Shigemitsu, Phys. Rev. D **86**, 034506 (2012) [arXiv:1202.4914 [hep-lat]].
- [55] A. Bazavov *et al.* [Fermilab Lattice and MILC Collaborations], Phys. Rev. D **85**, 114506 (2012) [arXiv:1112.3051 [hep-lat]].
- [56] N. H. Christ, J. M. Flynn, T. Izubuchi, T. Kawanai, C. Lehner, A. Soni, R. S. Van de Water and O. Witzel, arXiv:1404.4670 [hep-lat].
- [57] E. Gamiz *et al.* [HPQCD Collaboration], Phys. Rev. D **80**, 014503 (2009) [arXiv:0902.1815 [hep-lat]].
- [58] C. M. Bouchard, E. D. Freeland, C. Bernard, A. X. El-Khadra, E. Gamiz, A. S. Kronfeld, J. Laiho and R. S. Van de Water, PoS LATTICE **2011**, 274 (2011) [arXiv:1112.5642 [hep-lat]].
- [59] A. Bazavov, C. Bernard, C. M. Bouchard, C. DeTar, M. Di Pierro, A. X. El-Khadra, R. T. Evans and E. D. Freeland *et al.*, Phys. Rev. D **86**, 034503 (2012) [arXiv:1205.7013 [hep-lat]].
- [60] T. Blum, T. Izubuchi and E. Shintani, Phys. Rev. D **88**, 094503 (2013) [arXiv:1208.4349 [hep-lat], arXiv:1208.4349 [hep-lat]].
- [61] R. C. Brower, H. Neff and K. Orginos, Nucl. Phys. Proc. Suppl. **140**, 686 (2005) [hep-lat/0409118].
- [62] T. Blum, P. A. Boyle, N. H. Christ, J. Frison, N. Garron, T. zubuchi, T. Janowski and A. Juettner *et al.*, PoS LATTICE **2013**, 404 (2014).
- [63] G. Martinelli, S. Petrarca, C. T. Sachrajda and A. Vladikas, Phys. Lett. B **311**, 241 (1993) [Erratum-ibid. B **317**, 660 (1993)].
- [64] G. Martinelli, C. Pittori, C. T. Sachrajda, M. Testa and A. Vladikas, Nucl. Phys. B **445**, 81 (1995) [hep-lat/9411010].
- [65] T. Ishikawa, Y. Aoki, T. Izubuchi, C. Lehner and A. Soni, PoS LATTICE **2013**, 410 (2013) [arXiv:1312.1010 [hep-lat]].